Excitation and Readout of a Thermally Driven Time-Domain Optical Coherence Tomography System

Thesis report

May 27, 2010

Author:

M. Geljon B.Sc.
1143972

Supervisor and mentor:

Prof.dr. P.J. French
E. Margallo Balbás M.Sc.

TUDelft
Delft University of Technology

Challenge the future

Excitation and Readout of a Thermally Driven Time-Domain Optical Coherence Tomography System

Thesis report

May 27, 2010

Author:

M. Geljon B.Sc.
1143972

Thesis committee:

Prof.dr. P.J. French
Prof.dr.ir. G.C.M. Meijer
Dr.ir. R.F. Remis
E. Margallo Balbás M.Sc.

* The front page shows a close-up of the Thermo-Optical Delay Line (TODL) in an aluminium bracket. Connected to it are two optical fibres on the right and left side. Bond wires connect the TODL to the electronics.

Abstract

This system presented in this thesis report will be put into practice in a sensory system for dental drilling. The aim of this system is to provide real-time feedback to the practitioner about the anatomical structure in close vicinity of the drill bit. Therefore, the system has to deal with *in vivo*, *in situ* bone tissue, bone tissue within a living organism that cannot be removed from the human body for analysis. Hence, non-destructive biopsy is desired. Optical Coherence Tomography (OCT) imaging is able to provide optical biopsy at a high resolution and in real time. With the use of Optical Coherence Tomography (OCT), e.g. blood vessels, nerves and sinuses close to the drill can be detected before the drill bit does damage to these vulnerable anatomical structures.

Silicon process technology offers a promising platform for a relatively cheap Time-Domain Optical Coherence Tomography (TD-OCT) system. A first step into the direction of a single-chip TD-OCT system is the development of a thermally driven Optical Delay Line (ODL) or Thermo-Optical Delay Line (TODL). This thesis project is dedicated to the characterisation of the TODL in order to find the voltage excitation waveform that results in a linear variation in effective optical path length. By making use of the models, non-linearites can be compensated and the limited bandwidth can be extended by pre-emphasis of the voltage excitation waveform.

Two models are presented, based on the general heat equation for conduction. One model utilizes Fourier analysis to solve the heat equation and is a linear model by definition. The second model uses numerical methods and is able to incorporate non-linearities, such as relations for thermal conductivity, diffusivity and the variation of the refractive index of silicon as a function of temperature.

Measurements are conducted to verify the modeling. The linear model has been shown to perform poorly. The non-linear model was able to compensate for the non-linearities mentioned. However, first results showed that the TODL was behaving slightly slower than expected. The non-linear model was corrected for this behaviour by scalling down the relation for thermal diffusivity. The corrected non-linear model achieved a linear variation of the effective optical path lenght over a scanning range of $200\,\mu$m at a line scanning rate of $10\,$kHz.

Contents

Chapter 1

Introduction

To be able to define proper goals for this thesis project, one needs to have an understanding of why the Optical Coherence Tomography (OCT) system enhances the existing situation. This is explained in detail in section 1.1. The next step is to analyse the whole system and split the system into its core functions, section 1.2. This thesis work comprises the implementation of the electronics of the system, accommodated by two of the core functions. The core functions and the goals to be achieved are defined in section 1.3. Section 1.4 clarifies the outline of this report.

1.1 Motivation

Every year, over one million dental implants are placed in Europe. It goes without saying that this is a significant contribution to public health. However, this vast amount of implants implies that possible complications in implant placement affect a large number of patients.

Figure 1.1 shows an impression of a dental implant. To make room for the implant, a drill is used to remove sufficient bone tissue for the implant to fit in. This bone tissue encloses blood vessels and nerves, and this is where severe injuries can be caused. Injuries in the main vessels are considered a rare complication, but might have life-threatening impact. Injuries to the mental or lingual nerves induce a temporary or even permanent loss of ability to sense touch, heat and pain. Incidence of temporary sensory disturbances ranges from 1.7% to 43.5%, of which 0.3% to 19% persists after 1 year [1, 2]. Other surgical problems that trouble the practitioner are inadvertent perforation of the sinus membrane, leading to e.g. infections, and damage to adjacent teeth [2].

Figure 1.1. Impression of a dental implant

To avoid the complications mentioned above, the placement of any implant is preceded by a thorough planning phase. Firstly, radiographic images are taken to reconstruct a model of e.g. the patient's mandible. Imaging technology used for this purpose includes panoramic radiography, conventional tomography and Computed Tomography (CT). Nowadays, these systems are able to generate a three-dimensional model, usually based on information from a CT-scan. Figure 1.2(a) shows such a reconstructed model. With the help of this model and the raw CT-images, the position and angle of the implant are determined and added to the model (Figure 1.2(b)).
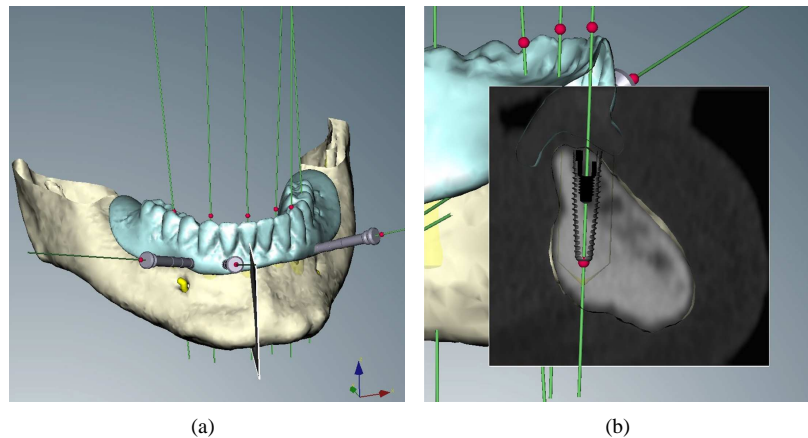

(a)   (b)

Figure 1.2. Computer aided design of a surgical guide (Nobel Biocare)

From this point on, the practitioner has a pretty complete view of the mandible, the implant and its surroundings. Using the model and the angles given by the practitioner, a surgical guide can be constructed to help the practitioner with the drilling. An impression of such a guide is given in Figure 1.3. However, such an aid provides guidance in only two dimensions. The third dimension, the depth, is left to the experience of the practitioner. As an example, the transition from cortical bone to trabecular bone comes with a rapid decrease of bone density. Care has to be taken here, as the drill behaves very differently from one instant to another. During the operation, the practitioner has to rely solely on the mental picture that he made according to the models generated during the planning phase. For this reason, implant placement requires practitioners with extensive training.
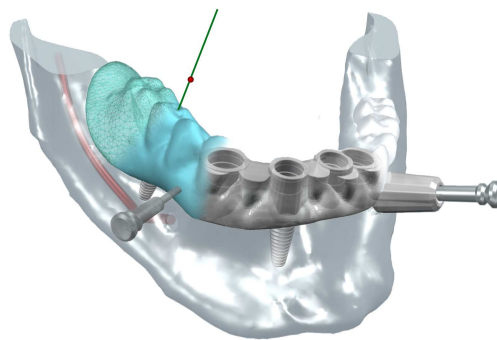
Figure 1.3. Impression of a surgical guide (Nobel Biocare)

In conclusion, as soon as the planning phase ends, there is no more feedback from the anatomy of the patient whatsoever. Today's imaging systems might be able to provide real-time feedback during surgery, but they lack the accuracy to be valuable in dental implantology. Another issue, especially with CT-scanning, is the amount of harmful radiation the patient is exposed to. The whole planning phase itself and the surgical aids are tailored to a specific patient, a costly and time consuming process. As with any system without feedback, such an approach is prone to errors and disturbances.

The aim of the dental drilling sensory system is to provide feedback during the operation phase. By early detection of vulnerable anatomical structures, the operator of the drilling system can be warned on beforehand. A measure for bone density gives the practitioner an idea about how much force should be applied to the drill. Hence, actual damage is less likely to occur and failure rates will be reduced. The sensory system has no need to be adjusted for a specific patient.

The two main requirements to such a warning system are thus a high spatial resolution and real-time scanning. Also, the system has to deal with *in situ* and *in vivo* bone tissue, bone tissue within a living organism that cannot be removed for analysis. Hence, non-destructive biopsy is desired. An OCT setup is able to provide optical biopsy at a high resolution and in real time. It was originally used to research retinae and coronary arteries [3]. Among many others, applications have been found in *in situ* bone tissue [4]. On top of that, the type of radiation used is not harmful, unlike existing X-ray imaging systems.

The OCT imaging system that is presented in this thesis report is based on fibre-optics and uses components that are widely used in telecom industry. In this way, OCT benefits from the fact that most components are widely available and well-documented.

Two types of OCT are available for this purpose. The difference between the two is in the way the depth-scan information is obtained. Time-Domain Optical Coherence Tomography (TD-OCT) gets its depth-scan information by varying the effective Optical Path Length (OPL) by means of an Optical Delay Line (ODL). By adjusting the delay of the optical signal in the reference arm, interference takes place with reflections from different depths in the tissue. To vary the delay, either the speed of light or the physical length of the optical path have to be tuned. The latter method is the most used and can be implemented by e.g. a scanning mirror. As these scanning methods are often relying on mechanical parts, the line scanning rate is rather low. The TD-OCT system will be discussed in more detail in section 1.2.

In the case of Fourier-Domain Optical Coherence Tomography (FD-OCT), depth-scan information is provided by an inverse fourier transformation of the spectrum of the backscattered light [5]. The depth-scan information is gathered through signal processing rather than a mechanical scanning method as in the case of TD-OCT. Systems based on FD-OCT generally have higher line rates than their TD-OCT compeers. A drawback of these FD-OCT systems is that they are based on tunable lasers and/or high-end photodetector arrays. These devices are rather costly and thus a high line scanning rate comes with a high price tag.

The key to a TD-OCT system is the ODL. Most ODLs are based on the variation of the actual length of the ODL, e.g. by a scanning mirror or by means of the piezo effect in certain materials. These methods provide scanning rates up to a few kHz [6]. What if we can increase the scanning rate of a TD-OCT system by introducing a thermally driven ODL, instead of a mechanical approach? The approach in the system proposed in this report is based on the influence of temperature on the refractive index of silicon, the thermo-optic effect. Advantages of a thermally driven ODL are that no moving parts are necessary and that the scanning rate is several orders of magnitude higher. Scanning rates of over $10\,kHz$ are reported [7].

The use of silicon provides a relatively cheap platform to incorporate compact photonic devices. Properties of silicon have been researched extensively and besides the electrical characteristics, a lot of knowledge is present about e.g. optical and thermal properties [8, 9, 10, 11, 12]. This enables the development of an ODL in silicon. Eventually, the TD-OCT system built around a thermally driven ODL achieves a high line scanning rate with substantially lower costs compared to FD-OCT.

1.2   Functional description

The sensing system is based on the TD-OCT setup as schematically drawn in Figure 1.4. The main function of this system is to irradiate bone tissue and analyse the reflections coming back from the bone tissue. The reflections contain information about e.g. tissue type, bone density and drilling speed in the direction of the drill.

The system can be explained best by following the optical signal from the source to the detector. A low-coherence light source generates an optical signal which is split among the sample arm and a reference arm by the optical coupler. The sample arm incorporates the rotary coupler and the drill bit. The rotary coupler
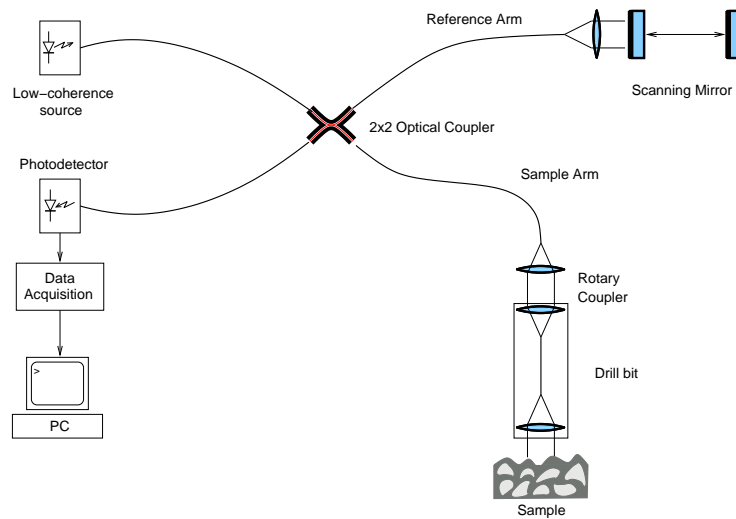
Figure 1.4. Schematical representation of OCT system

enables the coupling between the static drill and the rotating drill bit. By integrating an optical fibre into the drill bit of the dental drilling system, optical signals can be fed into the tissue surrounding the drill bit. Back-scattering or back-reflections of the optical signal on the tissue are picked up again by the fibre in the drill bit and come together with the signal that is reflected by the scanning mirror in the reference arm. When both optical signals meet in the optical coupler, interference occurs. As the source is low-coherent, interference only occurs if the OPL is equal in both arms. A controllable delay in the reference arm, in Figure 1.4 the scanning mirror, enables scanning over the depth range of the system. Hence, by varying the optical delay in the reference arm, interference is only present for reflections or scattering from a certain depth in the tissue. From the optical coupler, the interference pattern ends up at the photodetector.

Due to the rotation of the drill and the adjustable optical delay, the environment of the drill bit will be scanned in two dimensions. Finally, a digital representation of the implant's biological environment can be reconstructed by interpreting the optical information coming from the photodetector with the aid of an Analogue-to-Digital Converter (ADC) and digital signal processing.

1.3   Problem definition

The OCT imaging system as described in section 1.2 can be converted into the function block scheme depicted in Figure 1.5. The concern of this thesis project is to develop the electronics necessary to drive the OCT imaging system. The emphasis lies on the linearity of the acquired images. Once linearity is assured, further research can be put into real-time 2D imaging.

Apart from the low-coherent light source, the electronics involved in the OCT imaging system are made up by two subsystems. One subsystem controls the optical path length and the second preprocesses the optical output from the OCT imaging system. Both are highlighted in red in Figure 1.5 and will be explained in further detail in the following subsections.

Driving electronics for the thermo-optical delay line

The first subsystem addresses the variation of the Optical Path Length in the reference arm, to provide depth-scanning in the tissue of interest. This is covered by the function block 'vary Optical Path Length' in Figure 1.4. Although this subsystem is described by only one function block, it comprises the investigation of the interaction between three energy domains in order to find a linearly varying effective optical path length.
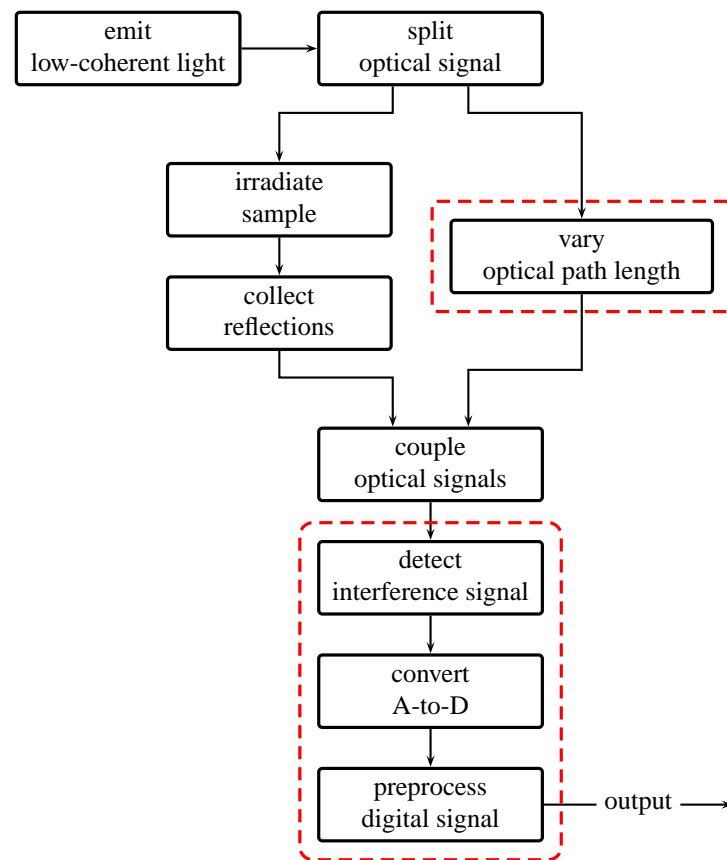
Figure 1.5. Function block scheme of the Dental Drilling Sensory System

The implementation of this function incorporates the modeling of the TODL and the design of the electronics necessary to regulate the effective optical path length of the TODL. To obtain a stream of pixels that is uniformly distributed in space over the depth-scanning range, the variation in OPL must be linear in the time domain. To verify the linearity, the model has to be tested by comparing the predicted behaviour to the measured behaviour.

As the ODL is thermally driven, the ODL is not able to follow discontinuities in the excitation signal. To avoid discontinuities, a triangular waveform is suggested. Hence, two scans are made during one period of the excitation signal. In conclusion, the process of modeling of the TODL, implementation and verification leads to part one of this thesis project as defined below.

> Design of a system to vary the effective optical path length according to a triangular waveform

Readout of the photodetector and image reconstruction

The second subsystem embodies the signal processing part of the system. The OCT imaging system provides an optical output signal. This optical signal has to be processed in such a way that it can be fed to a computer for further analysis and processing. Doing so, part two of this thesis project is defined:

> Signal processing of the optical interference signal to reconstruct a digital image

1.4   Organisation of this report

The report presents a method to manipulate the electrical input of the TODL to compensate for non-linearites in the optical output. By pre-emphasis of the electrical excitation, the limited bandwidth of the TODL can be extended significantly. In order to find the excitation waveform that eventually offers these benefits, the device has to be modeled. Chapter 3 presents two models, a linear model based on Fourier analysis and a non-linear model that utilizes a numerical partial differential equation solver. To verify the accuracy of the models, a measurement setup has been designed. Chapter 4 presents the electronics and the data acquisition designed by the author of this report, together with the optical components that are used. Finally, the response of two TODLs are analysed for a multitude of frequencies and ambient temperatures. Chapter 5 shows the results of the measurements taken. Conclusions and outlook follow in chapter 6

Chapter 2

Theory

Silicon provides a platform for compact optical systems and that is the reason why this material is of great interest when designing a Time-Domain Optical Coherence Tomography (TD-OCT) system. This chapter supplies the relevant theory behind a TD-OCT system and in particular, the Optical Delay Line (ODL) that forms the heart of this system.

The principles behind Optical Coherence Tomography (OCT) are explained in section 2.1. The need for an ODL is explained here, which leads to section 2.2. Section 2.2 takes care of a basic building block and work horse of the OCT system, the rib waveguide. The ODL will be driven in a relatively large temperature range compared to regular electronics. Especially when linearity over a wide temperature range comes into the picture, a thorough thermal analysis is required. Section 2.3 gives a glance upon the heat equation and introduces thermal diffusivity and thermal conductivity. The coupling between the thermal domain and the optical domain, the thermo-optic effect, lies at the basis of the whole system and is explained in section 2.4. Eventually, a close look has to be taken at the thermal diffusivity and thermal conductivity of silicon, given in section 2.4 as well.

2.1 Optical coherence tomography

OCT imaging is a type of optical imaging that emerged in the early nineties [3]. The system proposed by Huang in 1991[3] has been developed for noninvasive imaging in biological systems, tailored to retinae and coronary arteries. OCT performs high resolution, cross-sectional tomographic imaging of the internal microstructure in materials and biological systems by measuring backscattered or backreflected light. The use of low-coherence interferometry to produce an image of optical scattering or reflection from internal tissue microstructures is analogous to ultrasonic pulse-echo imaging.

Section 2.1.1 introduces the principles behind the OCT imaging system. Resolution and sensitivity will be discussed in section 2.1.2. Section 2.1.3 summarizes the various ODL's and their benefits and drawbacks.

2.1.1 Principles

In essence, OCT imaging is based on low-coherence interferometry of light waves. Two terms call for further explanation. Firstly, interferometry concerns the measurements of the superposition of two or more waves. In the case of OCT, the light waves which are reflected by e.g. a mirror and the biological tissue of interest interfere and produce an interference light wave. Secondly, the use of low-coherence light implies that interference only occurs when both waves have the same Optical Path Length (OPL).

Interference

A monochromatic light wave can be described by the wave equation 2.1, which expresses the electric field E of the wave. Substituting angular frequency ω and angular wavenumber κ according to equations 2.2, the wave equation can be rewritten as equation 2.3. The light wave is now a function of wavelength λ and refractive index n, with c the speed of light in vacuum and v_p the phase velocity of the wave. Furthermore, equation 2.3 shows that the refractive index only affects the temporal behaviour of the wave. The spatial behaviour remains unaffected.

$$E(x,t) = E_0 \cos \kappa x + \omega t \tag{2.1}$$

$$\kappa = \frac{2\pi}{\lambda} \qquad\qquad n = \frac{c}{v_p} \qquad\qquad v_p = \frac{\omega}{\kappa} \tag{2.2}$$

$$E(x,t) = E_0 \cos \frac{2\pi}{\lambda} x + \frac{2\pi c}{n\lambda} t \tag{2.3}$$

When combining the reference beam E_r and signal beam E_s, their fields add and produce interference. Mathematically, this is described as given in equation 2.4. A subsequent photodetector measures the output intensity of the interferometer I_o, which is proportional to the square of the electromagnetic field E. Taking into account the difference in OPL $\Delta l = l_r - l_s$, the intensity oscillates as a function of Δl [13]:

$$I_o(t) \propto \frac{1}{4}|E_{s0}|^2 + \frac{1}{4}|E_{r0}|^2 + \frac{1}{2}E_{s0}E_{r0} \cos 2\frac{2\pi}{\lambda}\Delta l \tag{2.4}$$

Low-coherence light

Coherence of a beam is a measure for the bandwidth of the light. Unlike a beam with a single wavelength or a very narrow bandwidth, low-coherence light is composed of a multitude of wavelengths. As a consequence of the interference between the spectral components, wave groups occur rather than one single propagating wave (Figure 2.1). No interference occurs when the Optical Path Lengths of the beam have a mismatch higher than the coherence length l_c. The coherence length l_c is inversely proportional to the bandwidth of the optical signal. Furthermore, the resolution of the OCT imaging system depends highly on the coherence length l_c.

Long Coherence Length Light   **Short Coherence Length Light**

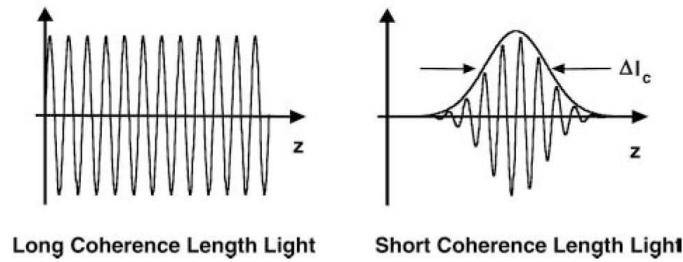**Figure 2.1.** low-coherence vs. high-coherence

Group velocity and phase velocity

In any non-monochromatic optical signal, the superposition of the individual waves will form wave groups. Such a wave group can be seen in the right half of Figure 2.1. Now there are two velocities to define, namely the phase velocity v_p and the grouph velocity v_g. In physical terms, the phase velocity is the speed in which

a certain phase front propagates. The group velocity defines the speed of the envelope of the wave group, i.e. the shape of the superposition. Both are in general not the same, unless the medium is non-dispersive.

The group velocity can be interpreted as the speed of the information in a signal and therefore this group velocity is of main interest in TD-OCT.

$$v_p = \frac{c}{n} = \frac{\omega}{\kappa} \qquad\qquad v_g = \frac{\partial\omega}{\partial\kappa} \qquad\qquad (2.5)$$

2.1.2 Resolution and sensitivity

One of the advantages of OCT is that the axial and transverse resolution are decoupled. The axial resolution is a function of the coherence length and thus of the bandwidth of the optical signal. Assuming a light source with a Gaussian spectral distribution, the axial resolution Δz is given in equation 2.6, where Δz and $\Delta\lambda$ are the Full Width at Half-Maximum (FWHM) of the autocorrelation function and power spectrum respectively. The centre wavelength of the source is given as λ_0. The axial resolution is inversely proportional to the bandwidth of the light source. Hence, broad-bandwidth optical sources have a short coherence lenght l_c and achieve high axial resolution [13].

$$\Delta z = \frac{2\ln 2}{\pi}\left(\frac{\lambda_0^2}{\Delta\lambda}\right) \qquad\qquad (2.6)$$

The transversal resolution is not dependent on the bandwidth of the light source. It is related to the minimum spot size to which an optical beam can be focused. This in turn is determined by the numerical aperture of the beam. The transversal resolution is given in equation 2.7, with λ_0 the wavelength or the light used, f the focal length and d the spot size on the objective lens [13].

$$\Delta x = \left(\frac{4\lambda_0}{\pi}\right)\left(\frac{f}{d}\right) \qquad\qquad (2.7)$$

In conclusion, the resolution is a function of the optical properties of the OCT system. The sensitivity however is merely a result of electrical properties of the detection system, as to be seen in equation 2.8. Firstly, the quantum efficiency η of the photodetector is a measure for the efficiency of the conversion from the optical domain to the electrical domain. Together with the power of the incident light P, this gives the electrical signal power. Secondly, the noise in the detector is proportional to the incident power P and introduces the noise floor of the system. Due to the proportionality, the noise is represented as the Noise Equivalent Bandwidth (NEB). Parameters h and v relate to the energy of a photon, with h the constant of Plank and v the velocity of the photon.

$$SNR = 10\log\left(\frac{\eta P}{2hvNEB}\right) \qquad\qquad (2.8)$$

2.1.3 Optical delay lines

In order to achieve depth scanning in a TD-OCT system, the propagation delay in the reference arm must be varied. If the propagation delay in the reference arm increases, interference will take place with reflections from deeper layers in the tissue. On the other hand, lower propagation delay will shift focus to reflections closer to the surface. Generally, an ODL is incorporated in the reference arm in order to control the propagation delay and thus the (effective) OPL.

To manipulate the propagation delay τ, equation 2.9 shows us two parameters to play with. That is, the length L of the optical path and the refractive index n of the material of which the optical path consists. The speed of light in vacuum c is a constant.

Most techniques are based on the variation of the OPL. The vast majority of these systems use a mechanical approach to obtain this variation. Linear actuators are reported, such as piezo-actuated mirrors [14] or piston-like structures to move a mirror back and forth [15]. Other approaches can be found in spinning mirror pairs [16] and piezo-actuated delay lines [17]. Due to the mechanical nature of these systems, the scanning rate is limited to the sub-1 kHz range.

$$\tau_g = \frac{distance}{velocity} = \frac{L}{v_g} = \frac{Ln}{c} \tag{2.9}$$

The other parameter, the refractive index n, allows a non-mechanical approach. By making use of the thermo-optic effect in silicon, light can effectively be slowed down by heating a silicon rib waveguide [7]. By modulating the temperature of the rib waveguide, a variable optical delay can be obtained. The thermo-optic effect is discussed in more detail in section 2.4.3.

2.2   Rib waveguides in silicon

A rib waveguide is a structure that confines light waves in two dimensions, similar to an optical fibre. The difference is that instead of a fibre, light is confined in a slab of silicon. How to achieve this confinement is explained in section 2.2.1. For research purposes, often a single-mode operation of the waveguide is required. This specifies the dimensions of the waveguide. The single-mode condition is covered in section 2.2.2.

The refractive index of silicon is not constant. Hence, the speed of light in silicon is a function of the wavelength. This implies that low-coherence light will smear out when travelling through silicon. This phenomenon is called chromatic dispersion and will be explained in further detail in section 2.2.3.

2.2.1   Confinement

In order to make a waveguide, light has to be confined in two dimensions. Confinement, in other words, means that light has to be reflected in all directions except for the preferred direction. By modeling the refractive index of the materials used, light can be guided into the preferred direction and hence a waveguide is obtained.

To get an understanding of confinement, one can have a look at the conditions for total reflection of a wave. Total reflection occurs when the angle of the incident wave θ_i exceeds the critical angle θ_c, given by equation 2.10. All angles are with respect to the normal of the boundary between the two materials. As silicon is the material of interest, n_0 can be substituted by the refractive index of silicon n_{Si}. To maximize the range of angles with total internal reflection, the critical angle should be as low as possible. Thus, the silicon waveguide should be surrounded by materials with a refractive index smaller than the refractive index of silicon $n_{Si} \approx 3.5$, preferrably as low as possible.

$$\theta_c = \arcsin\left(\frac{n_1}{n_0}\right) \tag{2.10}$$

The cross-section of a rib waveguide in silicon is shown in Figure 2.2. The waveguide is surrounded by two materials with refractive indices n_1 and n_2. The actual rib is shown with width w and height h. The ratio r defines the height h of the waveguide compared to the thickness of the surroundings. To obtain confinement in the direction normal to the silicon wafer, one usually uses Silicon-On-Insulator (SOI) wafers. In this case the surrounding materials would be air and/or silicon dioxide with $n_1 = 1$ and $n_2 \approx 1.5$ respectively. Although equation 2.10 gives insight in confinement, finding the conditions of confinement of a wave requires solving the Maxwell equations. A commonly used approach is the Effective Index Method (EIM), explained in chapter 2 of [8].
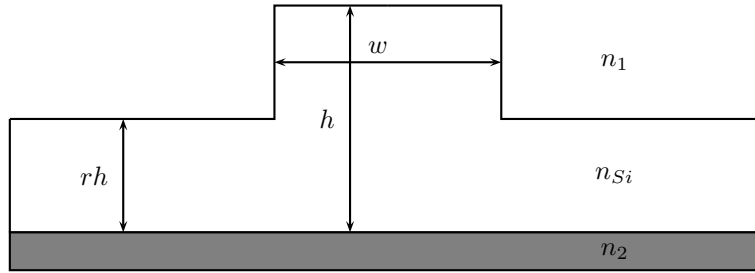
Figure 2.2. Rib waveguide geometry

Confinement in the lateral direction is such a case where equation 2.10 is not able to explain reflection. Although the refractive index of the material is equal in both the rib and the slab on each side, the propagation properties of a wave are affected by the geometry of the structure. These effects are taken into account by defining a so-called effective refractive index. The effective index is a function of the height h, the width w of the rib, the height rh of the planar section of the structure and the refractive index of the material. The factor r represents the ratio between the height of the slab and the height of the rib. Using the effective index method of analysis [8], one will find millesimal variations in the effective index. It is shown by Soref [18] that this is sufficient to confine light in the lateral direction. Hence, the rib structure on a SOI wafer achieves confinement in two dimensions, rendering a waveguide in silicon.

2.2.2   Single-mode condition

Fulfilling the single-mode condition is equivalent to stating that the effective refractive index of all higher order modes in the rib area should be lower than the effective refractive index of the fundamental mode in the slab region[19]. In terms of confinement, this means that for higher modes than the fundamental mode, the slab region no longer reflects the wave back into the rib section. Hence, higher order modes will leak away into the slab region.

By making use of the EIM, the effective refractive indices mentioned above can be evaluated. The geometry of the waveguide plays an important role is this evaluation. If the wavelength and refractive indices of the materials are given, the single-mode condition can directly be related to the dimensions of the waveguide as given in Figure 2.2. Soref made an approximation of this relation and came up with the unequality given in equation 2.11[10]. For waveguides with a height h greater than 4λ, he found a value of 0.3 for constant c. Pogossian compared equation 2.11 to experimental results found by Rickman [20], and adviced constant c to be 0 [19]. The single-mode conditions for both $c = 0.3$ (Soref) and $c = 0$ (EIM) are given in Figure 2.3. The dots and crosses refer to Rickman's experimental results with dots representing multi-mode waveguides and crosses representing single-mode waveguides.

$$\frac{w}{h} \leq c + \frac{r}{\sqrt{1 - r^2}} \tag{2.11}$$

What about the copyrights of figure 2.3?

2.2.3   Chromatic dispersion

Chromatic dispersion or intramodal dispersion results from the fact that the optical source used in TD-OCT is not purely monochromatic. The different spectral components of the source will have different propagation delays, for instance because the refractive index of silicon is function of wavelength. Also the geometrical properties of the waveguide structure on itself influences the propagation constant β. As a consequence, the envelope of the wave group will smear out, rendering the interference pattern wider than the coherence length Δl_c. In OCT, this means a loss of resolution.
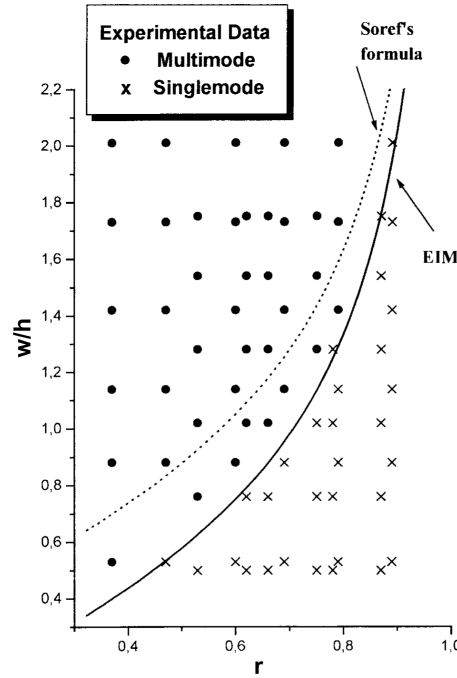
Figure 2.3. Single-mode condition compared to experimental data [19]

2.3 Heat conduction in solids

Heat transfer or transport of thermal energy is embodied by three phenomena, being convection, radiation and conduction. There is no convection in solids and radiative heat transfer is little at low temperatures. Given a temperature range up to $500\,\mathrm{K}$, transfer of heat in solids is thus dominated by conduction. Conduction in solids can be mathematically modeled by the general heat conduction equation, which is covered in section 2.3.1. When resistive heating is used to introduce energy into the system, one has to deal with Joule's first law as described in section 2.3.2.

2.3.1 General heat conduction equation

Thermal energy is subject to diffusion and thus heat will start to flow if a temperature gradient is present. For example, such a gradient occurs when heat is generated in, or added to a thermal system. Consequently, heat 'travels' from areas with high thermal energy to areas with lower thermal energy with a certain rate. In such a case, local temperature is a function of place and time.

Mathematically, an unsteady thermal system with external heat generation is described by the general heat conduction equation, given in 2.12. This equation originates from the conservation of energy and describes the spatial and temporal behaviour of heat conduction. Internal energy U represents the temperature at a certain location at a certain time instance. The generated heat q_{gen} takes into account heat that is added or extracted from the system. The thermal diffusivity α of a material is a measure for the rate of the heat flow. Another parameter of interest is the thermal conductivity k, which relates the power that is added to the system to a change in temperature.

$$\nabla^2 U(x,y,z,t) - \frac{1}{\alpha}\frac{\partial U(x,y,z,t)}{\partial t} = -\frac{1}{k}q_{gen} \tag{2.12}$$

2.3.2 Joule's law

Joule's first law, or Joule-Lenz law, relates the current flowing through a conductor to the generated heat in that conductor. Through Ohm's law, Joule's law can also be expressed as a function of the voltage across a conductor U. Both expressions are given in equation 2.13.

$$Q = I^2 R t \qquad Q = \frac{U^2}{R} t \tag{2.13}$$

The generated heat q_{gen} in equation 2.12 is the expressed as the power applied per unit of volume (W/m^3). Joule's first law relates the generated heat to the current and the electrical resistance of a conductor. This relation is given in equation 2.14, with Q the heat, V the volume, U the voltage across the conductor and R the resistance of the conductor.

$$q_{gen} = \frac{1}{V} \frac{\partial Q}{\partial t} = \frac{1}{V} \frac{U^2}{R} \tag{2.14}$$

2.4 Thermal properties of silicon

About any property of silicon is prone to variations with temperature. For use in a TD-OCT system, and in particular in a TODL, three of these properties are of interest. On one hand, there is the relation between the power applied to the silicon and the temperature of the silicon. The heating rate and magnitude are a consequence of the thermal diffusivity (section 2.4.1) and thermal conductivity (section 2.4.2) respectively.

On the other hand, there is the interaction between the actual temperature and the refractive index. This effect is called the thermo-optic effect and will be explained in section 2.4.3.

2.4.1 Thermal diffusivity

According to the heat equation, diffusion of heat will take place when a heat gradient exists in a material. The thermal diffusivity α of a material is a measure for the rate in which heat is conducted through that material. While this parameter is often assumed to be a constant, this does not hold for silicon in a large temperature range. As silicon has been an important material for the past decades, its diffusivity has been researched extensively. A few results are depicted in Figure 2.4. As to be seen in this figure, the curves have quite a spread, but their trend is similar. Although there is no concensus on the exact relation between thermal diffusivity and temperature, the general understanding is that the diffusivity is proportional to $T^{-1.8}$.

The measurements reported in Figure 2.4 were all conducted for bulk silicon. Heat conduction in silicon is dominated by phonon transport. In silicon layers, e.g. in SOI wafers, thermal conduction is expected to be lower than for bulk silicon, as several phonon scattering mechanism prohibit this transport [11]. On top of that, doping has its influence on phonon scattering mechanisms as well, which also implies a lower thermal diffusivity and the closely related thermal conductivity. For this reason, an approximation of Shanks' measurements is made, using the proposed proportionality $T^{-1.8}$ [12]. The approximation is fitted to the commonly used thermal diffusivity at room temperature and given in equation 2.15. Both Shanks' results and the approximation are depicted in Figure 2.5.
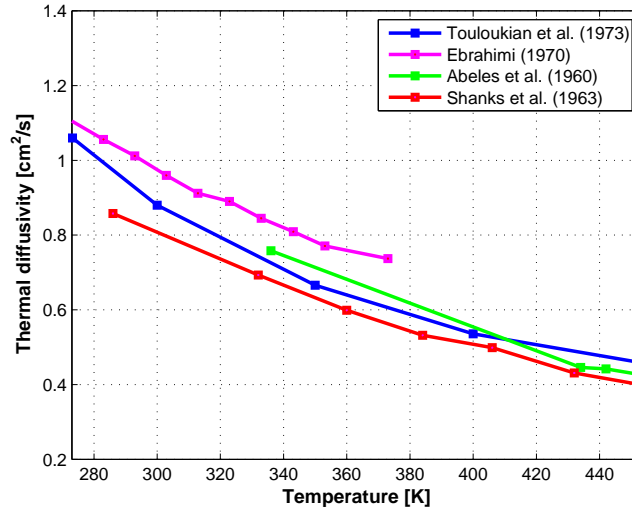
$$\alpha(T) = \frac{2.3106}{T^{1.8}} \tag{2.15}$$

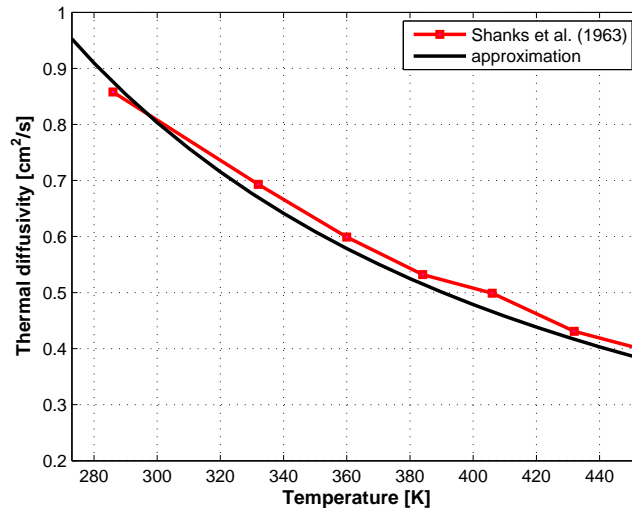**Figure 2.4.** Thermal diffusivity of silicon

Figure 2.5. Thermal diffusivity of silicon - an approximation

2.4.2 Thermal conductivity

Thermal conductivity k is defined as the product of density ρ, specific heat capacity c_p and thermal diffusivity α. Not only the thermal diffusivity, but also the specific heat capacity has its dependency on temperature. Because of this, the proportionality with $T^{-1.8}$ is not applicable here. The influence of the thermal expansion of silicon, i.e. the temperature dependence of the density ρ, on the thermal conductivity is reported to be less than 1%[12] and therefore neglected. Nonetheless, both dependencies are taken into account by Shanks. It can be seen from Figure 2.6 that a second order approximation fits Shanks' observations quite nicely. This approximation is given in equation 2.16 and will be used throughout this work.

$$k(T) \equiv \rho c_p \alpha \approx 7.88 \cdot 10^{-4} \, T^2 - 0.994 \, T + 370 \tag{2.16}$$
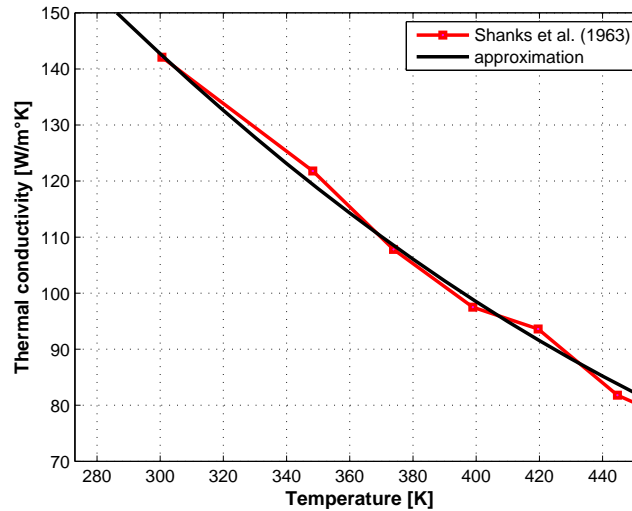
Figure 2.6. Thermal conductivity of silicon - an approximation

2.4.3 Thermo-optic effect

Given zero electric field, the relation between temperature and effective refractive index in silicon is dominated by two effects. Firstly, the carrier injection effect and secondly, the thermo-optic effect.

The refractive index in silicon is proportional to the electron concentration n_0 and hole concentration p_0. This phenomenon is called the carrier injection effect. Both electron and hole concentration are functions of the intrinsic carrier concentration n_i and the doping levels N_A and N_D. The intrinsic carrier concentration is strongly dependent on temperature [21, 22]. Figure 2.7 depicts the intrinsic carrier concentration n_i, the electron concentration n_0 and the hole concentration p_0 for the case that the donor concentration N_D is equal to 10^{14}. The carrier injection effect as a function of temperature can be calculated from these concentrations according to equation 2.17 [10].
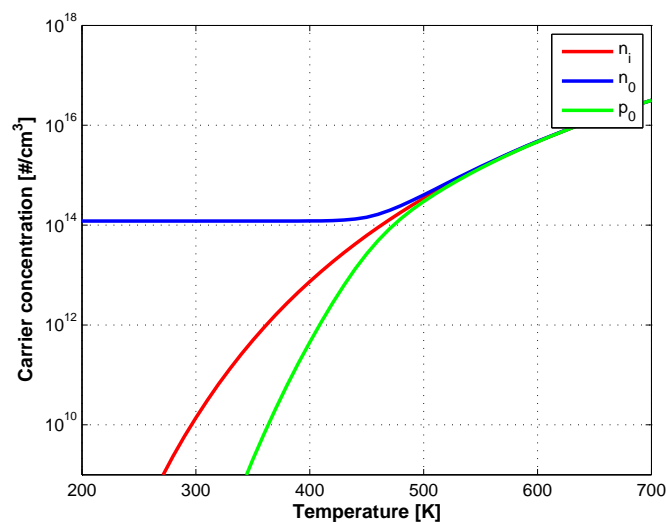
Figure 2.7. Carrier concentration as a function of temperature

For centre wavelength λ_0 equal to $1.3\,\mu$m:

$$\Delta n = \Delta n_e + \Delta n_h = -(6.2 \cdot 10^{-22}\Delta n_0 + 6.0 \cdot 10^{-18}(\Delta p_0)^{0.8}) \tag{2.17}$$

Also temperature has an influence on the refractive index of silicon, through the thermo-optic effect. According to Ghosh, the thermo-optic effect is attributed to thermal expansion and a variation of the excitonic band gap [23]. According to Moss' rule, the thermo-optic effect is related to the band gap energy, which in turn varies with temperature. Cocorullo summarized several theories and carried out measurements on a variety of samples with different crystal orientation and doping levels [24]. The second order model fitted to his findings is given in equation 2.18.

$$\Delta n(T) = \frac{\partial n}{\partial T} = -1.49 \cdot 10^{-10}\,T^2 + 3.47 \cdot 10^{-7}\,T + 9.48 \cdot 10^{-5} \tag{2.18}$$

However, Cocorullo's findings only consider phase velocity and are conducted for a wavelength of $1523\,$nm. Silicon is a dispersive material, hence the refractive index related to the phase velocity is different from the group refractive index. The relation given in equation 2.18 thus has to be corrected for the material dispersion. This is left for further research.

The conclusion to be drawn from equations 2.17 and 2.18 and Figure 2.7 is that the influence of the carrier injection effect is well below 1% of the thermo-optic effect in the temperature range below $600\,$K.

Chapter 3

Characterisation of the TODL

To provide undistorted images, a TD-OCT system depends on the linearity of delay variations in the ODL. Therefore, effort has to be put into linearising the delay variations when using such an ODL. The Thermo-Optical Delay Line is a device that operates across three energy domains. It is excited in the electrical domain, which affects the thermal domain and eventually results in modulation of the optical domain. This chapter describes the modeling of the TODL that enables the investigation of the trade-off between speed (line rate) and power consumption that is inherent to the TODL. On top of that, a method is presented to determine the electrical waveform that corresponds to the desired linearity in the optical domain.

The TODL structure and its dimensions are explained in section 3.1. The behaviour of the TODL in the three domains are treated seperately in sections 3.2 to 3.4. Sections 3.5 and 3.6 describe the linear and the nonlinear model respectively. Both models are compared in section 3.7. In section 3.8, the domains are put together to generate an excitation waveform for the TODL that will result in a linear variation of the optical delay.

3.1 The Thermo-Optical Delay Line, an overview

The principles behind the TODL are best explained by analysing its cross section. Its goal is to alter the group velocity of infrared light, i.e. a variable delay in the optical domain. The means to achieve this are based on rapidly heating up and cooling down of a silicon rib waveguide. The heating is provided by a platinum heater close to the rib waveguide, the cooling down is provided by a silicon membrane that is connected to the bulk silicon.

The base material for the TODL is a standard SOI wafer with a buried oxide layer of $375\,\mathrm{nm}$ thick. The monocrystalline silicon device layer is expanded to meet the height of the rib structure. After expansion, the n-type doping level is in the order of $10^{14}\,\mathrm{cm}^{-3}$. Calculations show that the carrier injection effect at this doping level introduces an error smaller than 0.1% compared to the thermo-optic effect, in the temperature range below $500\,\mathrm{K}$. Therefore, the carrier injection effect is neglected. The rib structure in the silicon is patterned using Reactive Ion Etching (RIE). The silicon membrane is fabricated by back-etching through the wafer up to the buried oxide. The cross section of the SOI wafer after the front- and back-etching steps is depicted in Figure 3.1. The slab region is $2.3\,\mu\mathrm{m}$ thick, while the rib itself has a height of $3.0\,\mu\mathrm{m}$. The width of the rib is $2.6\,\mu\mathrm{m}$. The length of the membrane is $10\,\mathrm{mm}$

From a modeling point of view, the device in Figure 3.1 can be split up into three parts. Each part represents the behaviour in one of the energy domains. A top-level model is presented in Figure 3.2. The electrical part of the TODL is a platinum heater structure. Two strips of platinum, the two blue rectangles in Figure 3.1, convert electrical energy into thermal energy through Joule's effect. A voltage $u(t)$ applied to the heater structure results in dissipation in the heater, the thermal power P_{th}. As the strips are placed close to the rib waveguide, the core of the waveguide will also heat up through heat conduction of the silicon
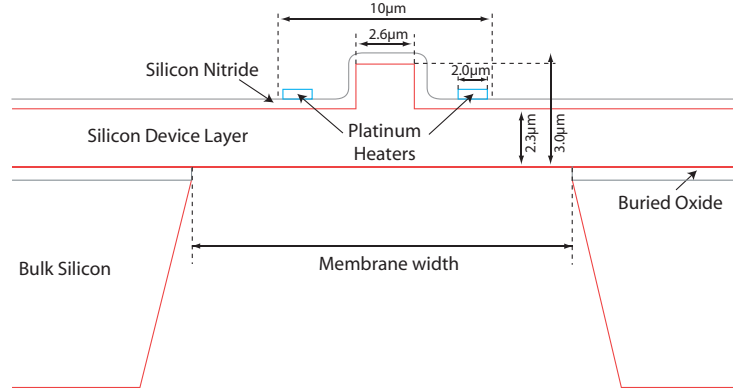
Figure 3.1. Cross section of the TODL

membrane. The membrane between the waveguide and the bulk silicon determines the relation between applied electrical power and the temperature of the core of the waveguide ΔT. In its turn, the silicon rib waveguide interacts with the thermal domain through the thermo-optic effect. A relative change in temperature with respect to the ambient temperature T_0 results in a change in the refractive index Δn. The change in refractive index directly influences the optical delay, here expressed as the effective path length Δl.
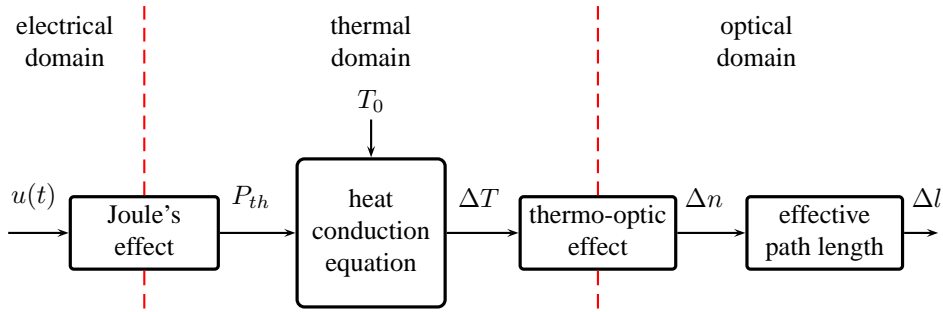

Figure 3.2. Top-level model of the TODL

3.2 Electrical domain, the platinum heater

The two platinum heaters are placed parallel to the waveguide. Both heaters span the whole length of the TODL, about $10\,\text{mm}$. Their measured resistance is approximately $7\,\text{k}\Omega$[25]. To facilitate driving the resistance with an off-the-shelf power amplifier, the resistance is brought down by decomposition of the heater into ten sections. A photograph of a single section is shown in Figure 3.3. Three materials can be recognised easily by colour. Silicon appears in purple, whereas platinum turns up in grey and a layer of gold is clearly distinguishable. The rib waveguide appears as a horizontal strip in slightly darker purple, in the middle of Figure 3.3. On either side of the waveguide is a narrow strip of platinum. These strips are connected at fixed intervals to a wider supply rail, also made of platinum. The supply rail is partly covered with gold to reduce the resistance. The heating structure is connected to the outside world through the layer of gold.

All ten sections are placed in parallel and the supply rails deliver the current to each section. Each supply rail is placed outside the membrane and has a resistance of $12\,\Omega$. The heater together with the supply rail can be modelled electrically by a lumped resistor network, shown in Figure 3.4. Each section of the heater is represented by a resistor R_H, the corresponding series resistance of the supply rail for each section is modelled as resistors R_s. The network is analysed using the Modified Nodal Analysis (MNA) method.
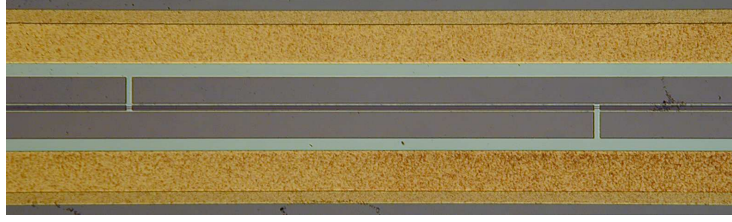
Figure 3.3. Photograph of a TODL (top view)

The MNA method is based on matrix calculations. Exploiting the periodicity of the network, MATLAB®️ creates the admittance matrix recursively. Calculations performed on the network in Figure 3.4 show that approximately 90% of the power applied is dissipated in the heater. The contact resistances R_c represent the connection from the supply rail to the contact pads. Parasitic capacitances and inductances are neglected.
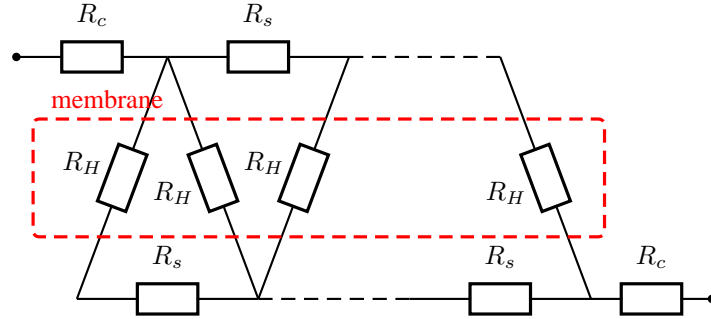

Figure 3.4. Electrical model of platinum heater

An advantage of the use of platinum is the reliability and stability over a wide temperature range. On top of that, it has a relatively high Temperature Coefficient of Resistance (TCR). This enables measurement of the temperature of the waveguide by measuring the resistance of platinum. As the TCR of platinum is known to be lower for thin films than for bulk platinum, calibration measurements are taken in a controlled temperature oven. The resistance of the platinum structure depends linearly on temperature with a positive coefficient of $\alpha_{pt} = 2230\,\text{ppm/K}$. The actual resistance R is given by equation 3.1 with ΔT the temperature with respect to ambient temperature and R_0 the resistance of the platinum structure at ambient temperature. Due to the parallelisation of sections, R_0 is reduced from $7\,\text{k}\Omega$ to about $80\,\Omega$.

$$R(T) = (1 + \alpha_{pt}\Delta T)R_0 \tag{3.1}$$

According to Joule's law, equation 2.13, the generated heat is a linear function of the resistance of a conductor. The thermal power P_{th} generated by the current flowing through a conductor, the platinum heater, is then the first time derivative of Joule's law, given in equation 3.2. Because of the losses in the supply rails of the heater, the thermal power is multiplied by 90 %.

$$P_{th}(t) = \frac{\partial Q}{\partial t} = \frac{u(t)^2}{R(T)} \cdot 90\% \tag{3.2}$$

3.3 Optical domain, the rib waveguide

The cross section of the TODL in Figure 3.1 shows a structure that is similar to Figure 2.2, in the middle of the membrane. However, to ensure the functioning of the structure as a waveguide that is suitable for OCT, one has to evaluate confinement and the single mode condition. Without confinement, light is scattered

along the whole silicon device layer, rendering a well defined manipulation of the light impossible. Multiple modes will cause multiple interference patterns, which might even overlap eachother. This complicates the detection of the right interference pattern. Multiple interference patterns reduce resolution and produce multiple images.

The dimensions of relevance for the optical behaviour are the heigth h and width w of the rib and the ratio r between slab region thickness and the rib heigth as defined in Figure 2.2. These dimensions determine whether there is confinement and if the single-mode condition is fulfilled. Whereas the optical behaviour is determined by the cross section of the waveguide, the beam is exposed to this behaviour for the whole length of the waveguide. The length of the waveguide L_y is $10\,\text{mm}$. The total delay is thus obtained by integrating the optical behaviour along the optical path in the TODL.

Confinement is evaluated using the Effective Index Method (EIM). A graphical representation of the single-mode condition, equation 2.11, is repeated here as Figure 3.5 with the TODL marked as a red cross. The figure shows that the TODL is well into the region where both the conditions proposed by Soref and Pogossian [18, 19] as well as experimental data by Rickman [20] predict single-mode operation.
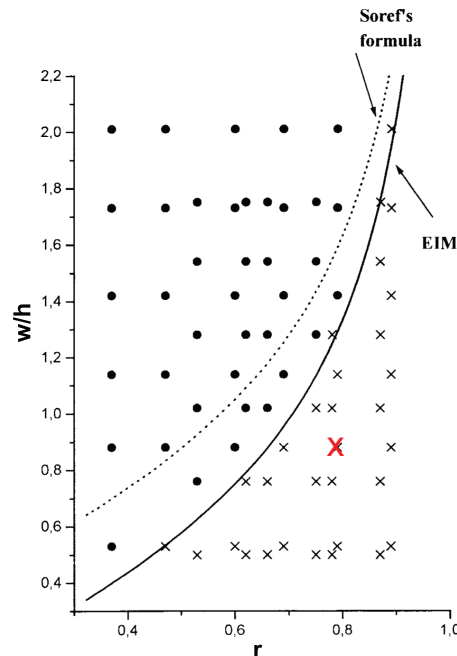

Figure 3.5. Single-mode condition compared to experimental data (adapted from [19])

The difference in refractive indices of air and silicon causes a considerable amount of light to be reflected back from any silicon-air-interface. A fraction of the incident light will thus be reflected back and forth through the waveguide. This enables the option to produce interference with light that has travelled through the waveguide multiple times. The scanning depth of the OCT system is linearly proportional to the total delay added by the TODL, compared to the delay in silicon at ambient temperature. The advantage of multiple reflections is that the beam passes the active part of the TODL several times. The delay of a single pass is thus multiplied by the number of reflections. The main drawback of using multiple reflections is a lower signal-to-noise ratio, as part of the optical power is lost in every reflection.

In conclusion, the additional OPL is obtained by integrating the change in refractive index Δn over the total physical path length. The change in refractive index caused by the thermo-optic effect is given in equation 2.18. The temperature at a certain point in the waveguide follows from the thermal modeling in section 3.4. The additional OPL then follows from equation 3.3. The additional OPL of a single pass can also be expressed as the average change in refractive index $\Delta \bar{n}$ over the waveguide times the length of the waveguide L_y. This value has to be multiplied by the number of reflections N to obtain the total change in

OPL.

$$\Delta l(t) = \int_{OPL} \Delta n \, dl = N(\Delta \bar{n} L_y) \tag{3.3}$$

3.4   Thermal domain, the silicon membrane

The main function of the silicon membrane between the rib waveguide and the bulk silicon is to increase the thermal resistance to the bulk silicon. Besides that, the reduction in mass of the waveguide means a lower thermal capacitance. This enables faster heating and cooling down of the waveguide.

To acquire a basic understanding of the thermal behaviour, one can have a look at the simplified electrical equivalent of the membrane, shown in Figure 3.6. This circuit is merely meant to support the explanation of the thermal behaviour. The three masses in the system, being the bulk silicon on both sides of the membrane and the membrane itself, are modeled as capacitances C_{th}. The rate of the heat flow between the masses is modeled as thermal resistances R_{th}. To introduce the heat flow $\frac{dQ}{dt}$ into the system, a current source provides thermal power P_{th} to the circuit via the node that represents the membrane temperature. When the source is on, heat is accumulated in the membrane. A temperature difference is built up in $C_{th,membrane}$. The temperature difference across thermal resistances R_{th} results in a heat flow from the membrane into the bulk. The membrane in combination with the bulk silicon thus acts as a low-pass filter in the thermal domain. The centre of the membrane, where the rib waveguide is, only experiences the high-frequency part of the thermal power signal. The bulk silicon capacitances $C_{th,bulk}$ are considered sufficiently big to filter only the DC-component of the thermal power signal.
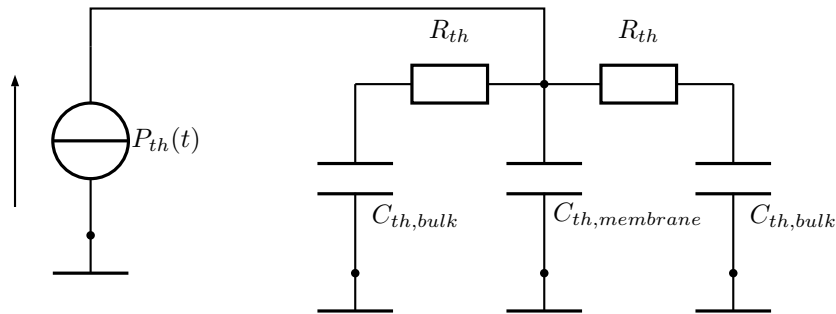

Figure 3.6. Electrical equivalent of the silicon membrane

Regarding the thermal behaviour, the relevant dimensions from Figure 3.1 are the membrane width, the membrane length and the height of the slab region, i.e. the silicon device layer . Whereas the membrane length and the height of the slab region are fixed, a variety of TODLs is available with different membrane widths. The membrane width affects both the speed of the device and the power necessary to reach a certain temperature. A relatively wide membrane has a high thermal resistance to the bulk, which implies that heat is flowing to the bulk slowlier. Hence, a higher temperature is built up in the membrane, but this is at the cost of speed. The membrane cannot cool down fast enough. For a narrow membrane, the effect is opposite. More power is needed to reach the same temperature, but the device can be driven at higher frequencies. Therefore, a trade-off between speed (line rate) and power is inherent to this device.

Investigation of this trade-off and eventually finding the proper excitation signal requires a more sophisticated model. The membrane can be looked at as a slab of silicon with the same dimensions as mentioned in section 3.1. Figure 3.7 shows a slab of silicon with membrane length L_y and width L_x. The two platinum heaters are modeled as a single strip in the middle of the membrane, the red line in Figure 3.7. Doing so, the thermal resistance between the platinum heaters and the silicon membrane are neglected. Furthermore, the membrane is considered to be thin compared to its length and width. Temperature difference in the z-direction is assumed to be zero, which reduces the membrane to a 2D model.
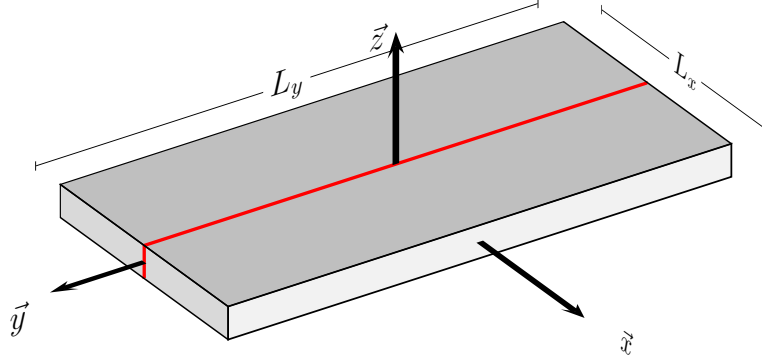
Figure 3.7. Simplified silicon membrane

As stated in section 2.3.1, heat transfer in solids is dominated by conduction. Convection and radiation are neglected. With the given assumptions, the silicon membrane can now be represented by the general heat conduction equation (eq. 2.12), adapted to 2D (eq. 3.4). In this equation, $U(x,y,t)$ is the temperature with respect to ambient temperature T_0. The applied power P_{th} appears in the equation as $q_{gen}(x,t)$ through the 2D equivalent of equation 2.14, given in equation 3.5. The power is only present at the y-axis in Figure 3.7 and therefore has to be multiplied by the Dirac delta pulse $\delta(x)$ in the model. The thermal conductivity and diffusivity are represented by α and κ respectively. Substitution of the voltage excitation waveform $u(t)$ and the platinum resistance $R(T)$ from equation 3.1 completes the model.

$$\nabla^2 U(x,y,t) - \frac{1}{\alpha}\frac{\partial U(x,y,t)}{\partial t} = -\frac{1}{k}q_{gen} \tag{3.4}$$

$$q_{gen}(x,t) = \frac{1}{A}P_{th}(t)\delta(x) = \frac{1}{L_y L_z}P_{th}(t)\delta(x) \tag{3.5}$$

The solution to this differential equation represents the thermal behaviour of the membrane. In order to find the particular solution, initial conditions and boundary conditions have to be defined. The initial condition, given in equation 3.6, states that the whole membrane is at ambient temperature T_0 at $t=0$. The boundary conditions are chosen such that the sides of the membrane are at ambient temperature at any time instance. The boundary conditions are expressed mathematically in equations 3.7.

$$U(x,y,0) = 0 \tag{3.6}$$

$$
\begin{aligned}
U(-\frac{L_x}{2},y,t) = 0 \quad & U(\frac{L_x}{2},y,t) = 0 \\
U(x,-\frac{L_y}{2},t) = 0 \quad & U(x,\frac{L_y}{2},t) = 0
\end{aligned}
\tag{3.7}
$$

3.5   Linear model: Fourier analysis

A linear solution to equation 3.4 can be found using Fourier analysis, as it was originally developed to solve the heat equation. Exploiting the assumed linearity, it is convenient to determine the step response of the membrane. Equation 3.8 represents a step input to the system, with P_0 the power per area, $\delta(x)$ the Dirac delta pulse which defines the location of the heater and $\epsilon(t)$ the Heaviside step function. The generated heat q_{gen} has to be substituted in the heat equation from equation 3.4. The differential equation can then be solved by evaluating the Fourier series given in equations 3.9 and 3.10 [25]. For the thermal conductivity κ and diffusivity α, the constants at room temperature are used, being $\kappa = 148\,\mathrm{W/mK}$ and $\alpha = 0.8\,\mathrm{cm^2/s}$.

$$q_{gen} = P_0 \, \delta(x)\epsilon(t) \tag{3.8}$$

$$D_{mn} = \begin{cases} 0 & \text{for } m \text{ odd or } n \text{ odd} \\[2ex] \dfrac{8P_0(-1)^{(m-1)/2}}{n\pi\kappa L_x \left(\dfrac{m^2\pi^2}{L_x^2} + \dfrac{n^2\pi^2}{L_y^2}\right)} & \text{for } m \text{ even and } n \text{ even} \end{cases} \tag{3.9}$$

$$U_{gen}(x,y,t) = \sum_{m=1}^{\infty} \sum_{n=1}^{\infty} D_{mn} \cos\left(\frac{m\pi}{L_x}x\right) \cos\left(\frac{n\pi}{L_y}y\right) \left[1 - e^{-\alpha\pi^2\left(\frac{m^2}{L_x^2}+\frac{n^2}{L_y^2}\right)t}\right] u(t) \tag{3.10}$$

The step response as a function of merely time is found by averaging the temperature along the rib waveguide at $x = 0$. The input power P_0 is set to $\frac{1}{L_y L_z}\text{W/m}^2$. This represents an applied power of $1\,\text{W}$. The step response is expressed mathematically in equation 3.11.

$$H(t) = \frac{1}{L_y} \int_{-\frac{L_y}{2}}^{\frac{L_y}{2}} U_{gen}(0,y,t)dy \Bigg|_{P_0 = \frac{1}{L_y L_z}\text{W/m}^2} \tag{3.11}$$

With the step response at hand, the temperature response to a certain excitation in thermal power $P_{th}(t)$ is found by convolution of the latter with the impulse response, the time derivative of the step response, equation 3.12.

$$\Delta\bar{T}(t) = \frac{d}{dt}H(t) * P_{th}(t) \tag{3.12}$$

Finally, the average temperature change $\Delta\bar{T}(t)$ can be translated into a change in effective OPL. Equation 3.13 is equal to equation 3.3 after substitution of the constant for the thermo-optic effect at room temperature $\frac{\Delta n}{\Delta T} = 1.86 \cdot 10^4$.

$$\Delta l(t) = N(1.86 \cdot 10^4 \Delta\bar{T}(t)L_y) \tag{3.13}$$

Summarizing, the function block scheme from Figure 3.2 is implemented by substituting equation 3.2 into equation 3.12 and subsequently substitution into equation 3.13.

Frequency response

To find the step response, equation 3.10 is evaluated with 20 odd modes in the x-direction and 100 odd modes in the y-direction. Doing so, a 2D thermal map of the silicon membrane is obtained. The part of interest is the temperature along the waveguide, being the solution $U_{gen}(0,y,t)$. Figure 3.8 shows the steady-state response $U_{gen}(0,y,\infty)$ for TODLs with different membrane widths. As expected for a linear model, the shape is the same for all membrane widths, the amplitude is scaled as a function of width.

The step response is found by averaging the temperature along the waveguide for every time instance t. The step responses for a number of membrane widths are displayed in Figure 3.9. Here, the power-speed trade-off is clearly visible. The wide membrane in red delivers a temperature change that is much higher than the narrower membranes in green and blue. The time to reach steady-state however is much longer than for its narrower compeers.

The impulse response for a specific membrane forms the heart of the linear model, but does not show the power-speed trade-off as clearly as the step response. Therefore, the step response is displayed here. The iteration process does use the impulse response.
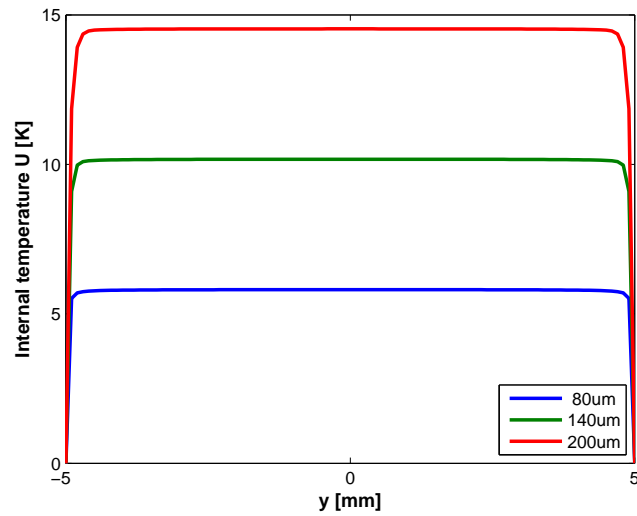
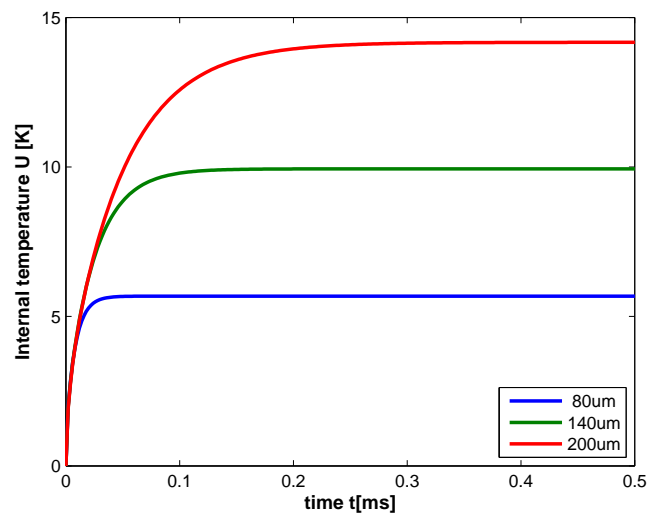**Figure 3.8.** Temperature along the waveguide

Figure 3.9. Step response of TODL

Advantages

The linear model gives the designer a good basic understanding of the thermal behaviour of the membrane. The response is qualitatively right and allows the use of methods for further analysis such as a bode plot. This gives a worst-case approximation in terms of power and gives a good estimate of the membrane's thermal cut-off frequency.

The Fourier series only has to be evaluated once to find the step response. Once the step response is calculated, the iteration process is fairly easy in terms of computing power. The iteration frequency is thus higher than for the non-linear case.

Limitations

The main limitation of the Fourier analysis is that this approach does not allow non-linear variables by definition. However, Figures 2.5 and 2.6 show that both the thermal diffusivity and the thermal conductivity drop by approximately 25 % over an increase in temperature from room temperature to $100\,°\text{C}$. The decrease in conductivity implies a lower required power, although the speed of the device is reduced due to a lower diffusivity.

Furthermore, the ambient temperature is not taken into account. Bulk heating might increase the steady-state temperature of the membrane edges and in practice, room temperature changes from day to day. This cannot be accounted for in the linear model.

In conclusion, the non-linearity of the thermal conductivity and diffusivity has a significant effect on the thermal behaviour of the TODL. This justifies a closer look at the non-linearities and the development of a non-linear model.

3.6 Non-linear model

For the non-linear model, a numerical approach is more suitable. For this purpose, the Partial Differential Equation (PDE) solver `pdepe` in MATLAB®is used. The PDE solver enables the use of the non-linear equations described in section 2.4.

The function `pdepe` is a 1D solver and thus more assumptions have to be made. Comparing the average temperature change $\Delta\bar{T}$ with the maximum temperature change at $(x, y) = (0, 0)$ in Figure 3.8 tells us that the discrepancy between the two is a mere 2%. Neglecting this discrepancy is equivalent to the statement that the membrane is a segment of an infinitely long membrane. The temperature profile along the x-direction would be the same for every value of y. U_{gen} is now no longer a function of y and we are left with a 1D model.

To be able to use the solver, the heat equation from equation 3.4 has to be rewritten in the form that is imposed by the PDE solver, equation 3.14. Therefore, equation 3.4 has to be multiplied by κ. Now, variables c, f, s correspond to equations 3.15-3.17. The parameter m represents the symmetry of the problem. In this case, m is equal to zero, which implies slab symmetry. The thermal conductivity $\kappa(T)$ and diffusivity $\alpha(T)$ are given in equations 2.16 and 2.15. Using equation 3.18, the internal temperature U can be related to the absolute temperature T. Also, the ambient temperature T_0 is taken into account here.

$$c\left(x, t, U, \frac{\partial U}{\partial x}\right)\frac{\partial U}{\partial t} = x^{-m}\frac{\partial}{\partial x}\left(x^m f\left(x, t, U, \frac{\partial U}{\partial x}\right)\right) + s\left(x, t, U, \frac{\partial U}{\partial x}\right) \tag{3.14}$$

$$c = \frac{\kappa(T)}{\alpha(T)} \tag{3.15}$$

$$f = \kappa(T)\frac{\partial U}{\partial x} \tag{3.16}$$

$$s = \frac{1}{L_y L_z}P_{th}(t)\delta(x) \tag{3.17}$$

$$T = 273 + T_0 + U \tag{3.18}$$

With c, f, s and m, the boundary conditions and the initial conditions defined, a mesh of x and t has to be fed to PDE solver `pdepe` . The mesh specifies the points at which a numerical solution is requested. The thermal power waveform $P_{th}(t)$ is passed on internally in MATLAB®. Figure 3.10 shows the output of `pdepe` , $\Delta T(x, t)$, for $P_{th}(t) = 10\,\epsilon(t)$, a step function of $10\,\text{W}$. The characterised membrane width L_x is $80\,\mu\text{m}$.
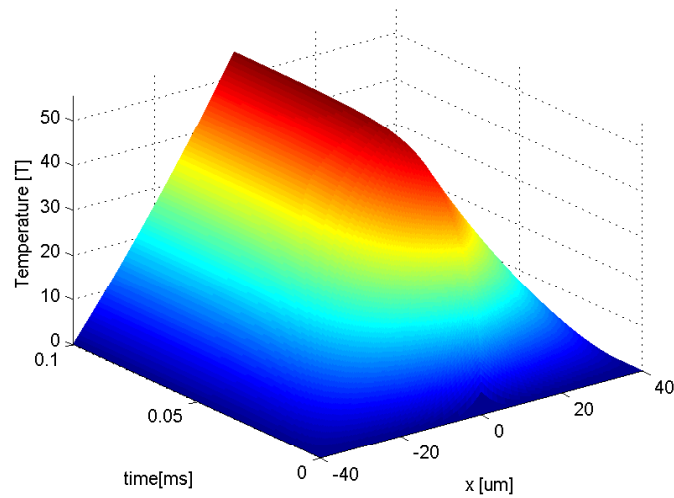
Figure 3.10. Solution $\Delta T(x, t)$ provided by `pdepe`

As the averaging over the membrane length is replaced by an assumption in the non-linear model, the response of the membrane is the solution given by the PDE solver for all $x = 0$. A response similar to the step response for the linear model is achieved. Figure 3.11 shows the response for a range of ambient temperatures for a $80\,\mu\mathrm{m}$ membrane excited with a $10\,\mathrm{W}$ step.
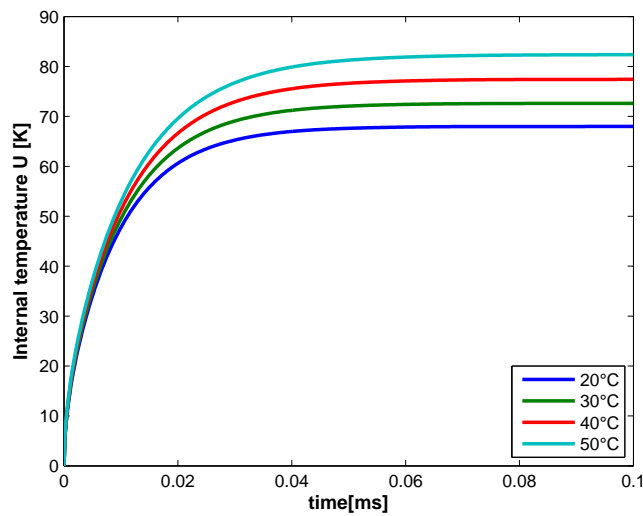

Figure 3.11. Membrane response versus ambient temperature

Summarizing, the non-linear implementation of the function block scheme from Figure 3.2 consists of feeding equation 3.2 to the PDE solver and subsequently substituting the results into equation 2.18 and 3.13.

3.7   Comparison

With both models implemented, the behaviour of the two can be compared regarding power requirements and speed. For the platinum heater, there is no difference between the two models as there is no further information available about the heater. Introducing the second-order approximation of the thermo-optic effect results in a deviation up to 10 % compared to the constant at room temperature. The non-linearity shows up in the thermal modeling as the thermal conductivity and diffusivity. The first mainly affects the steady-state behaviour, whereas the latter influences the membrane response in terms of time.

The thermal conductivity is known to decrease for an increase of temperature. A raise in temperature results in a higher temperature change for the same amount of power applied. Hence, the power-temperature interaction enforces itself. Figure 3.12 shows the steady-state behaviour for a membrane with a width of $80\,\mu$m. A step of $10\,$W in thermal power is used for simulation. With a power of $10\,$W, a temperature range is covered that is close to the expected operating range of the TODL. The figure shows a non-linear steady-state temperature which is 20 % higher than for the linear model. For a wide membrane, $160\,\mu$m, simulations show a difference of 50 %. The cause for the bigger impact for wider membranes lies in the fact that higher temperatures are reached for the same power excitation. If the ambient temperature is increased from room temperature to $40\,°$C, the difference increases to 30 % for a $80\,\mu$m wide membrane.
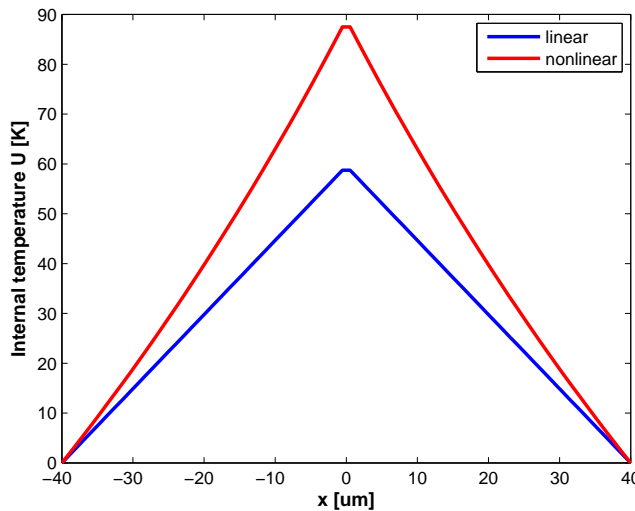

Figure 3.12. Steady-state behaviour

Both models show the power-speed trade-off. The non-linear model should show itself a little slower, as the thermal diffusivity goes up for increasing temperatures. Figure 3.13 depicts the response of the $80\,\mu$m wide membrane, again for a step input. However, the power is equalised in such a way that the steady-state values match. The linear model has a step input of $10\,$W, for the non-linear model a power step of $8.5\,$W suffices. If we define the response time as the time it takes to reach the steady-state behaviour within $1\,\%$, the non-linear model is about 30 % slower. For a membrane of $160\,\mu$m wide, this percentage goes up to 70 %. In this case, the percentages are more a qualitative comparison, as they deviate a lot for different margins.
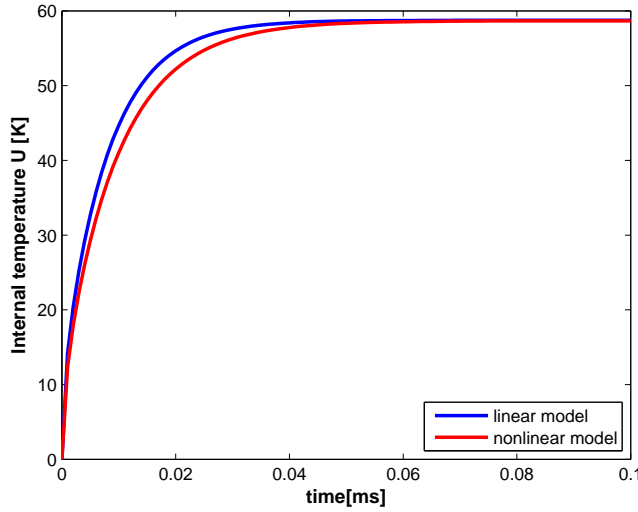
Figure 3.13. Membrane response with equalised steady-state behaviour

3.8   Waveform generation

Sections 3.2 to 3.4 describe the set of equations that have to be solved in order to find the voltage excitation signal for a given optical behaviour. However, it is not straight-forward to reverse the general heat conduction equation with non-linearities. On top of that, temperature depends on power through the heat equation and power depends on temperature through the temperature dependency of the platinum heater. Therefore, a solution is found by means of an iteration process.

The solution is based upon the desired behaviour in the optical domain. Section 3.8.1 introduces the ideal waveform and states the requirements to the voltage excitation waveform. The iteration process is presented in section 3.8.2. Results of the iteration process are shown in section 3.8.3.

3.8.1   Waveform requirements

To serve its purpose, the TODL has to modulate the optical delay linearly in time at a certain frequency. Non-linearities in the optical delay result in distortion in the image. The range of the delay determines the scanning range in the tissue. The frequency relates directly to the line scanning rate.

The TODLs under test have a power limitation of about $20\,\mathrm{W}$. This puts a limit to the scanning range and the frequency. To obey the power limitation over all the model parameters, the scanning range to set to $200\,\mu\mathrm{m}$. The change in OPL Δl represents the instantaneous scanning depth. For ambient temperature, Δl is zero and thus the scanning range is equal to the maximum value for Δl that can be achieved. Combining the scanning range and the linearity requirement, the ideal change in effective OPL $\Delta l_{ideal}(t)$ is found. Figure 3.14 shows the ideal case for two excitation periods. As the object of interest can be scanned on both the rising flank and the falling flank, the line rate is twice as high as the excitation frequency.

The generated voltage excitation waveforms consist of one hundred samples per excitation period. The accuracy to be achieved in the iteration process is set to 7 bits. The maximum error between the ideal waveform and the calculated waveform that results from the final voltage excitation waveform is thus less than $0.8\,\%$.

To characterise the frequency behaviour of the TODL, a variety of excitation frequencies is applied. First of all, the maximum line scanning rate is expected to be a function of the membrane width. Second, the gain-bandwidth product of the photodetector limits the bandwidth of the optical signal to $5\,\mathrm{MHz}$. To perform all
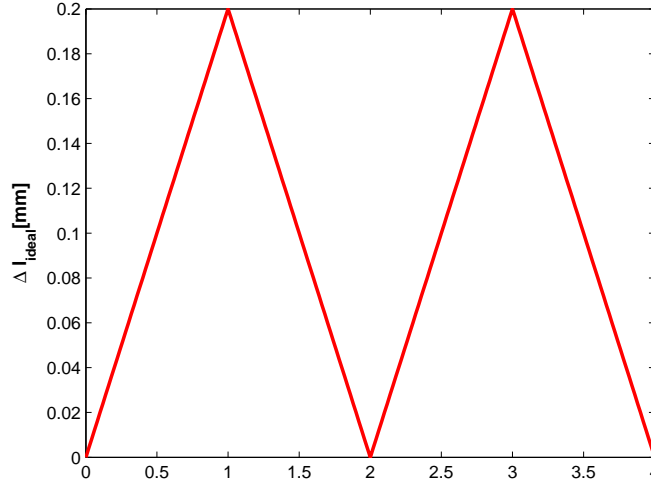
Figure 3.14. Ideal optical behaviour

measurements with the same measurement settings, the maximum line scanning rate is set to $10\,\mathrm{kHz}$. The maximum excitation frequency is thus $5\,\mathrm{kHz}$.

The waveform requirements stated in this section also impose requirements on the Digital-to-Analogue Converter (DAC) that eventually provides the waveform to the TODL. The DAC should have a sample rate of $100\,f_{exc,max} = 500\,\mathrm{kSPS}$ or bigger. The minimum resolution in bits is 7.

The waveform requirements mentioned in this section are summarized in Table 3.1.

Parameter		min	max	range	
Scanning range	Δl_{max}			200	um
Line scanning rate	f_s	2	10		kHz
Excitation frequency	f_{exc}	1	5		kHz
Accuracy				0.8	%
DAC frequency	f_{DAC}		≥ 500		kSPS
DAC resolution		7			bits

Table 3.1. Waveform requirements

3.8.2 Iteration process

For both models, the same iteration process is used. The iteration cycle, based on Figure 3.2, is shown in Figure 3.15. The iteration process starts with waveform $u_0(t)$. In theory, any waveform can be chosen for $u_0(t)$, but the process benefits from an 'educated guess' in terms of speed. By using the waveform from Figure 3.14 and the constants for the thermo-optic effect and thermal conductivity k_0 at room temperature, a first estimate is found. Equation 3.19 calculates $u_0(t)$, depending on TODL dimensions L_x, L_y and L_z and the resistance at room temperature R_0.

$$u_0(t) = \sqrt{\frac{\Delta l_{ideal}(t)}{1.86 \cdot 10^4 \, L_y} \frac{4k_0 L_y L_z}{Lx} \frac{R_0}{90\%}} \tag{3.19}$$

Figure 3.15 represents the iteration process in the form of a Function Block Scheme. From waveform $u_0(t)$, the first iteration of $\Delta l_i(t)$ is calculated using the set of equation in sections 3.2 to 3.4. $\Delta l_i(t)$ is
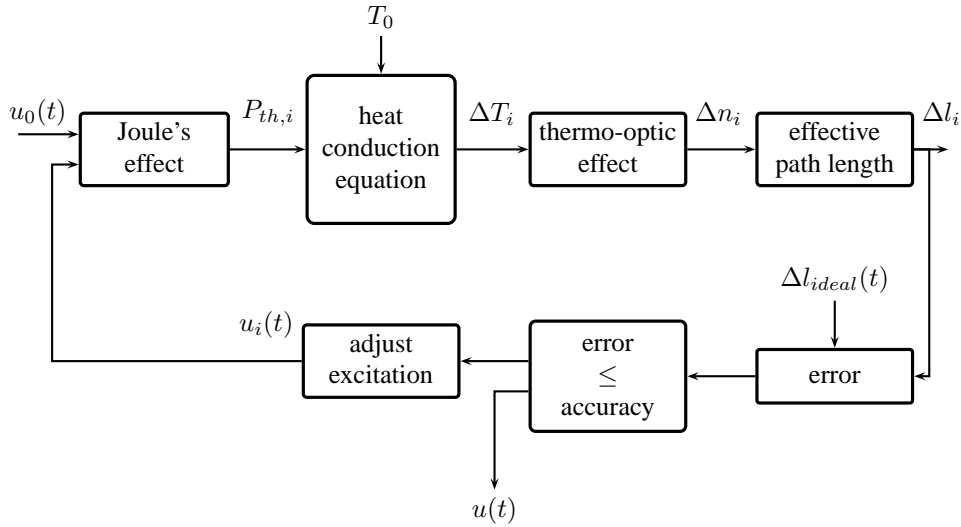
Figure 3.15. Function block scheme of the iteration cycle

compared to $\Delta l_{ideal}(t)$ in the block 'error'. The next block checks whether the imposed accuracy is met or not. If not, the last voltage excitation waveform $u_{i-1}(t)$ is corrected for the error and fed back into the set of equations as $u_i(t)$. When the maximum error is greater than 10 %, $u_{i-1}(t)$ is scaled to match the overall gain from voltage to effective OPL. When the maximum error is less, $u_{i-1}(t)$ is reshaped according to the instantaneous error $e(t)$. Eventually, the iteration process ends when a voltage excitation waveform $u(t)$ is found that meets the accuracy.

3.8.3   Characterisation results

The iteration process from section 3.8.2 is able to generate the voltage excitation waveforms according to the requirements specified in section 3.8.1. The input parameters are the membrane width L_x, the excitation frequency f_{exc} and the ambient temperature T_0. For frequencies below 500 Hz, all membranes are able to follow the shape of a square-rooted triangular waveform suggested in equation 3.19, only the gain of the waveform has to be adjusted for. For higher excitation frequencies, the membrane can no longer follow the excitation waveform. This manifestates itself especially at the moments where the waveform is not smooth, i.e. where the spectral components at high frequencies dominate. This has to be compensated for.

Figure 3.16 shows three waveforms for a membrane width of $80\,\mu\mathrm{m}$ and an excitation frequency of 5 kHz. The line scanning rate is thus 10 kHz. This example shows the most extreme case, as the wider membranes are not able to be operated at such a high excitation frequency. The waveforms for wider membranes would look similar, except the voltage is lower. The blue waveform is the suggested excitation considering a linear model. One can see that the iteration process emphasises the higher spectral components by suggesting a step-like behaviour at the moments where the ideal waveform is not smooth. The red waveform considers a non-linear model. Here the amplitude is corrected for the reduced thermal conductivity and diffusivity at high temperatures. Also, the emphasis on high frequencies is even stronger. The green waveform is a square-rooted waveform that is meant for comparison with the excitation waveform for a membrane with an infinite thermal bandwidth.

The iteration process is finished when a certain accuracy is met. Figure 3.17 shows the error for the waveforms in Figure 3.16 after the accuracy is met. Inherent to the iteration process, the maximum error is equal to $\frac{1}{2^7}$ for both. For apparent reasons, the error is the largest at the moments where the ideal waveform is not smooth.

In conclusion, the square-rooted triangular waveform that originates from the quadratic relation between power and voltage, equation 2.13, only holds for low excitation frequencies and relatively narrow membranes. For higher frequencies and wider membranes, the poor high-frequency behaviour has to be compensated for by pre-emphasis of the excitation waveform. The ambient temperature has a positive effect on the required power in the sense that less power is needed when the ambient temperature is high. On the other hand, the maximum excitation frequency of the device goes down and one has to keep in mind the power necessary to raise the ambient temperature.
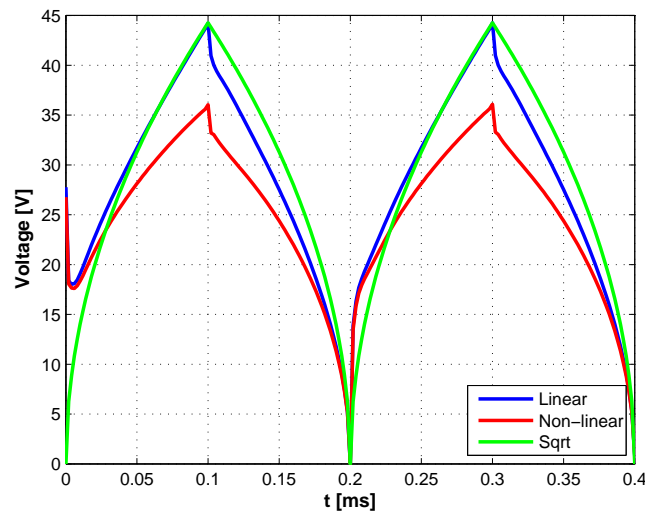

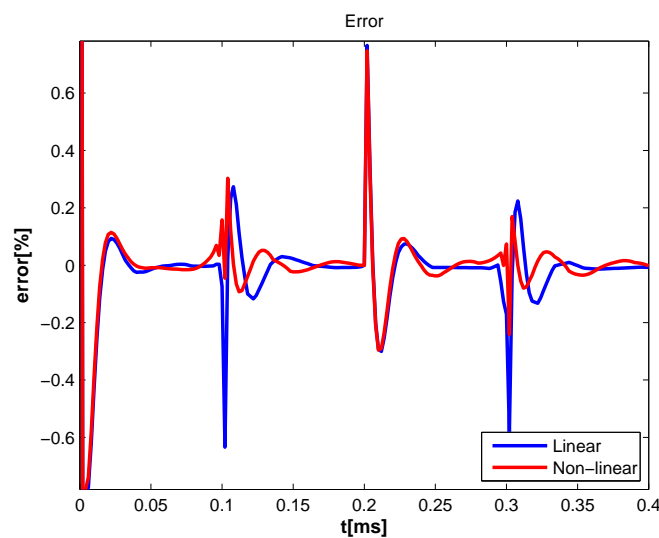**Figure 3.16.** Excitation waveforms (5 kHz)

Figure 3.17. Error between generated and ideal waveform

Chapter 4

Material and methods

To verify the model that is proposed in chapter 3, measurements will be done on several TODLs with a variety of membrane width, excitation frequencies and ambient temperatures. This chapter describes the measurement setup, its components and the methods used to obtain the measurement data. Section 4.1 gives a quick overview of the measurement setup in comparison with the OCT system described in section 1.2. Sections 4.2 to 4.4 explain the details of the hardware and software designed for this purpose. The optical components that are used are described in sections 4.5 to 4.8.

4.1 Functional description of the measurement setup

The measurement setup is an adaption of the system explained in Figure 1.4. The TODL replaces the optical parts related to the drill bit. The scanning mirror is now a reference for measurements on the TODL. The TODL is continuously excited by a voltage signal that is determined in section 3.8. The mirror covers a range of positions with a fixed step size. Analysing the interference patterns for every position of the mirror unveils the scanning range of the TODL and its linearity. To obtain information about the membrane temperature and power consumption, the instantaneous voltage and current are monitored by the readout electronics. The acquired data from the photodetector and the readout electronics are synchronised and pre-processed before transmission to a Personal Computer (PC).
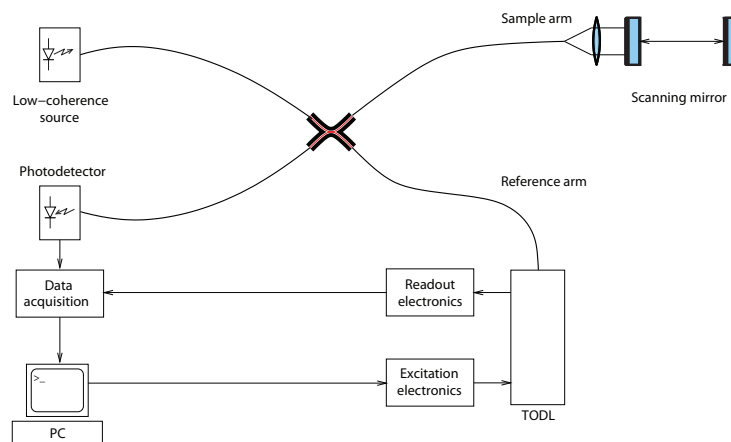

Figure 4.1. Schematical representation of the measurement setup

The measurement setup is designed to execute measurements autonomously. The PC controls, either directly or via the data-acquisition-board, all the electronics and the position of the scanning mirror. Measurements are taken by a single mouse-click.

4.2   Excitation electronics

To put the characterisation of the TODL to practice, the generated voltage excitation waveform has to be translated from a vector in MATLAB® to an analog voltage signal. A Digital-to-Analogue Converter (DAC) connected via the Universal Serial Bus (USB), section 4.2.1, makes the step from software to hardware. A power amplifier, section 4.2.2, adds power to the signal such that the generated voltage waveform appears over the TODL.

4.2.1   Digital-to-Analog-converter

A Data Acquisition module (DAQ) from National Instruments (NI USB-6259) is used in the measurement setup as a DAC. It connects to a PC via USB and offers a variety of analog and digital in- and outputs. The analog outputs offer 16 bits of resolution and a sample rate of $2.8\,\mathrm{MSps}$. Compared to the requirements in section 3.8.1, this is more than enough.

The DAQ communicates directly with MATLAB®. In MATLAB®, a few scripts are written to start, stop and select the proper voltage excitation waveform plus the corresponding sample frequency. The scripts pre-scale the excitation waveform, such that the output voltage range of the DAQ is met. The waveform is therefore divided by the gain of the power amplifier. Hence, the voltage waveform after amplification meets the vector values in MATLAB®.

4.2.2   Power amplifier

The voltage excitation waveforms presented in section 3.8.3 require voltages up to $45\,\mathrm{V}$. The TODL acts as a resistive load of about $80\,\Omega$ and thus the peak current lies around $0.7\,\mathrm{A}$. As both the output voltage range and the current sourcing specifications of the DAQ do not fulfill these requirements, the DAQ is not able to drive the TODL. The function of the amplifier is to increase the power of the voltage signal that is supplied by the DAQ.

The power amplifier is based on the OPA548T, a high-voltage, high-current operational amplifier by Texas Instruments. The minimum gain necessary to match the voltage range of the excitation to the voltage range of the DAQ is $4.5\mathrm{x}$. Before taking measurements, the gain is calibrated by comparing the peak output voltage of the amplifier to the excitation waveform in MATLAB®. The peak output voltage is measured with help of the voltage cursors on a Tektronix TDS2014B oscilloscope. The pre-scale factor, which should be close or equal to the gain of the amplifier, is tuned until the peak output voltage matches the peak voltage of the excitation waveform. The pre-scale factor used for the measurements in chapter 5 is $4.81\mathrm{x}$.

4.3   Readout electronics

The readout electronics deals with the acquisition of the electrical signals, the voltage across and the current through the TODL. Section 4.3.1 states the two pitfalls that have to be avoided when measuring resistance. To measure the electrical quantities while the TODL is also connected to the optical system has some implications on the mechanical aspects of the measurement setup. The interfacing of the TODL with both electrical and optical signals requires some mechanical design, section 4.3.2. The two Printed Circuit Board (PCB) designs are clarified in sections 4.3.3 and 4.3.4.

4.3.1 Measurement problem

Two of the problems of measuring TODL resistance are the resistance of the measurement wires and a phase mismatch between voltage and current. The measurement wires have parasitic resistance, capacitance and inductance. To some extent, measurement wires might even work as antennas and pick up any form of electro-magnetic waves. The most relevant parasitics are considered to be the resistance and inductance. To minimize the measurement error, wires have to be short and thick. The measurands have to be amplified as close as possible to the object to measure.

Any capacitive or inductive behaviour will cause a phase shift between the voltage and the current. In the case of the voltage excitation waveform given in Figure 3.16, the voltage goes down to almost zero. This results in a current that is almost equal to zero too. When the resistance is calculated by division of the voltage by the current, according to Ohm's law, the phase mismatch induces in large errors. Figure 4.2 shows the impact of $1°$ phase mismatch for triangular voltage and current signals. The simulated resistance is defined in equation 3.1 with R_0 equal to $80\,\Omega$.
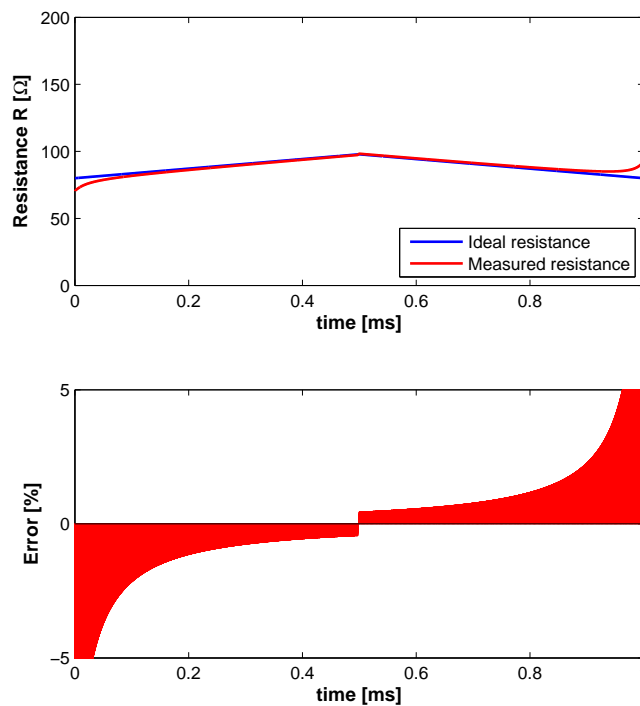

Figure 4.2. Effect of a $1°$ phase mismatch between voltage and current

The conclusion to be drawn from Figure 4.2 is that resistance measurements are prone to large errors at low voltages when a phase mismatch is present. Hence, adding an offset to the voltage excitation waveform will improve the resistance measurement. On the other hand, adding static power to the device changes the temperature response. In case the static power raises the ambient temperature, the amplitude of the voltage excitation waveform with respect to the offset level is slightly lower. This makes up for part of the added power that results from the applied offset voltage. Nonetheless, the total required power to retain the same scanning range will increase.

The voltage offset improves the resistance measurement, but it might affect the optical behaviour in a negative way. The best way to obtain decent resistance measurements is thus to minimize the phase difference between voltage and current.

4.3.2   Mechanical design

The TODL has both optical and electrical in- and outputs. Two optical fibres have to be aligned with the rib waveguide for optical coupling. To optimize the alignment, the TODL is placed on a rotational stage and the location of the two optical fibres is controlled by two XYZ-stages. The TODL cannot be operated on the rotational stage, as the stage cannot sink the heat that is dissipated in the TODL. The temperature of the rotational stage was measured at $60\,^{\circ}\text{C}$ under steady-state excitation. Therefore, operation of the TODL requires a heatsink. Furthermore, the accuracy of the resistance measurements benefits from circuitry that is close to the TODL. On the other hand, this circuitry may not obstruct the optical fibres.

A variety of TODLs have to be tested. It is therefore convenient to design two PCBs. One PCB is mounted near the TODL to exploit the advantage of being close to the device. Every TODL comes with its own PCB. This TODL-board contains few components, so that the extra effort to test more TODLs is small. The majority of the components are placed on a second PCB, the readout-board. To overcome the mechanical and thermal problems, a metal bracket is designed that can be mounted in the rotational stage. A large heatsink is equipped with a similar mount, such that the bracket can be placed onto the heatsink after alignment. The bracket has an elevated plateau for the TODL. The surroundings of the plateau are used to fit the TODL-board. With the top of the PCB aligned to the bottom of the TODL, the optical fibres are not obstructed. The electrical connections are made by wire bonding the TODL directly to the TODL-board. Figure 4.3 shows a photograph of the TODL, the bracket and the TODL-board on the rotational stage used for alignment. The main optical fibre on the left is glued into place with epoxy. The optical fibre on the right is used for checking the alignment of the main fibre. After the main optical fibre is fixated, the fibre on the right is removed and the TODL-board is electrically connected to the readout-board through the carde-edge connector on the right.

Figure 4.3. Aluminium bracket, the TODL-board and a TODLmounted on a rotational alignment stage for fixation of the optical fibre

4.3.3   TODL-board

The aim of the TODL-board is to minimize the error introduced by the wire resistance, by means of a four-point measurement with short wires. The phase mismatch is minimized by applying the same circuitry in both signal paths. Figure 4.4 shows a simplified schematic design of the TODL-board. The voltage excitation signal is applied via clamps $P+$ and $P-$, which are connected to the power amplifier from section 4.2.2. A fraction of this voltage appears at the node in the middle of R_T and R_B. The current through the TODL causes a voltage across the sense resistor R_{SENSE}, present at the node between R_{TODL} and R_{SENSE}. Both resistor pairs act as a voltage divider with a ratio of 1:1000. The voltage at the

nodes describes are subsequently amplified by a differential amplifier based on the OPA365 from Texas Instruments. Using the amplifier in a differential configuration allows both a single-sided and symmetric excitation of the TODL. This adds to the flexibility of the measurement setup. The differential amplifier offers a gain of 21x.
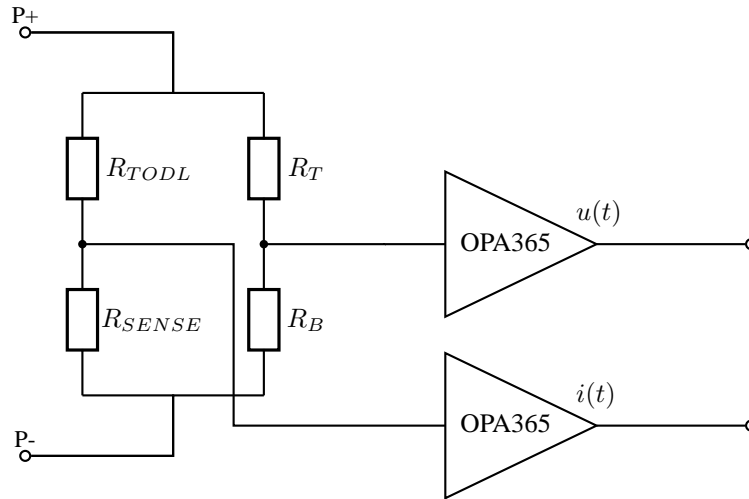

Figure 4.4. Simplified schematic design of TODL-board

The supply voltage of $\pm 2.5\,\text{V}$ comes from the readout-board. Furthermore, the board contains a number of test-pads, which give access to vital signals. In Figure 4.3, a top view of the TODL-board is shown. The top half consists of the test pads, the sense resistor R_{SENSE} and two golden pads where the bond wires can be attached. The bottom half of the board houses two opamps OPA365 in a single package, their feedback networks and capacitors for power supply stabilisation.

4.3.4 Readout-board

The purpose of the readout-board is to address the phase mismatch and to apply time multiplexing of the voltage and current signals. The data acquisition board discussed in section 4.4.1 offers only one ADC for electrical signals. Therefore, the ADC has to be shared between the two signals.

The simplified schematic design of the readout-board is depicted in Figure 4.5. The two signals $u(t)$ and $i(t)$ represent the signals coming from the TODL-board in Figure 4.4. To avoid any further phase difference, both signals are sampled by a Sample-and-Hold Amplifier. The two active-low 'HOLD'-signals are provided by the data-acquisition-board. If necessary, a phase mismatch can be (partly) compensated for by adding a delay between the two 'HOLD'-signals. The time multiplexing is implemented by a high-speed switch, which follows the S&H Amplifier. The data-acquisistion-board provides the 'SWITCH'-signal. The next step is to match the voltage range of the signal to the input voltage range of the ADC. The amplifier has a variable gain between 1.6x and 13x. The gain stage following the switch also compensates the 50 % voltage loss for impedance matching. The offset voltage is selectable, either $0\,\text{V}$ or $2.5\,\text{V}$, depending on whether the TODL is driven single-sided or symmetrically.

The symmetrical power supply of the readout-board is a Delta E018-0.6D, which supplies $\pm 15\,\text{V}$ to the board. The readout-board has on-board voltage regulators to provide $\pm 12\,\text{V}$ for the readout-board itself and $\pm 2.5\,\text{V}$ for the TODL-board. The active components that make up the readout-board are summed up in Table 4.1. A photograph of the readout-board is presented in Figure 4.6.

The total delay in the components used, together with the sampling rate of the ADC, determine the maximum sample rate that the readout-board can deliver. With the digital design presented in section 4.4, the maximum sample rate is $500\,\text{kSps}$. At the maximum excitation frequency of $5\,\text{kHz}$, the readout provides

100 samples per excitation period. This is equal to the number of samples that is generated by the DAC and therefore sufficient. Every sample consists of a value for voltage and a value for current. Gain-phase analysis of the readout-board is available in appendix 6.
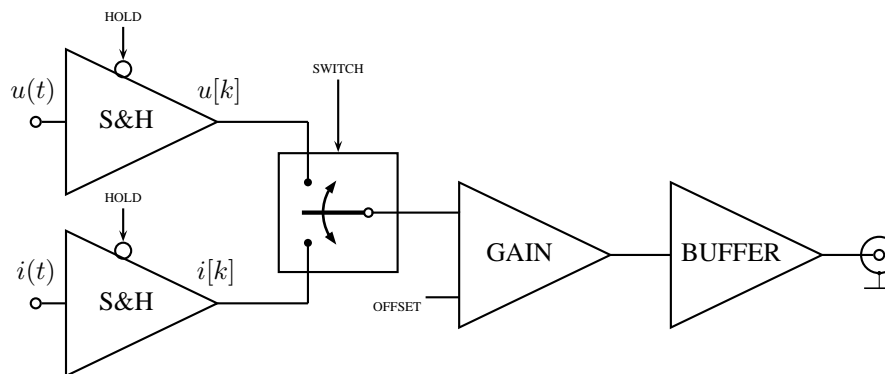

Figure 4.5. Simpflified schematic of readout-board

Function	Manufacturer	Product code
Sample-and-Hold Amplifier	Analog Devices	AD781
Switch	Vishay	DG642
Differential Amplifier	Analog Devices	AD8130
Buffer Amplifier	Intersil	HA-5002
Voltage Reference	Texas Instruments	ref50XX
Voltage Regulator $\pm 12\,\mathrm{V}$	National Semiconductor	78M12/79M12
Voltage Regulator $\pm 2.5\,\mathrm{V}$	National Semiconductor	LM317LZ/LM337LZ

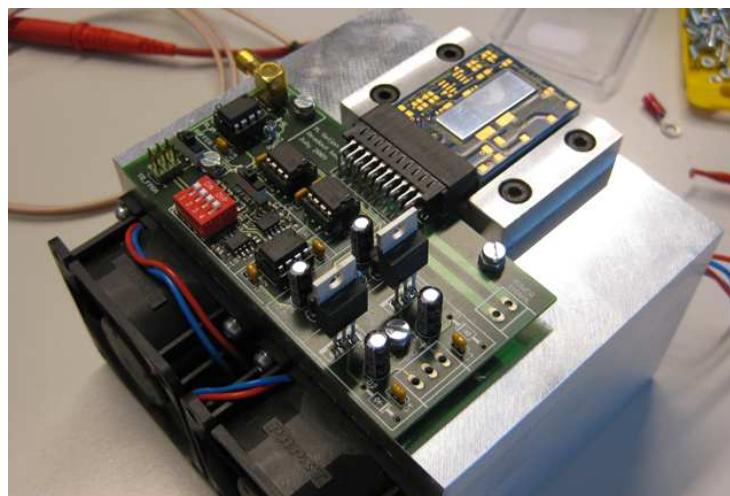**Table 4.1.** Active components on the readout-board

Figure 4.6. Readout-board on a large heatsink with a dummy bracket and TODL-board installed

4.4 Data acquisition

In essence, the data acquisition part of the measurement setup makes the transition possible from the analogue, time-continuous world to a world of vectors and matrices that can be manipulated by the PC. The data-acquisition-board has two on-board Analogue-to-Digital Converters, which quantise and discretise the analogue signals coming from both the readout-electronics as well as the photodetector. The board is discussed in more detail in section 4.4.1. The digital signals from the ADCs are fed to a Field-Programmable Gate Array (FPGA). The FPGA is programmed to control the data acquisition process and to support a USB data connection to the computer. The optical signal is pre-processed in the FPGA as well. Section 4.4.2 explains the design of the digital hardware. The top-level control of the measurement process, data analysis and visualisation of the acquired data are taken care of by a script in MATLAB®, section 4.4.3.

4.4.1 Data-acquisition-board

The basis of the data-acquisition-board is the XEM3005 integration board from Opal Kelly. Among others, it features a Xilinx Spartan-3E FPGA, a Phase-Locked Loop (PLL), a USB-interface and two expansion connectors. The digital hardware design from section 4.4.2 is uploaded to the FPGA via the USB-interface. The PLL is also configured via USB and generates two clock signals. One for the electrical data acquisition and another one for its optical counterpart. The integration board from Opal Kelly connects to the data-acquisition-board via the two expansion connectors.

Apart from the power supplies, the data-acquisition-board contains two Analogue-to-Digital Converters by Texas Instruments. An ADS804 is used for conversion of electrical signals. It features 12-bit resolution and $10\,\mathrm{MSps}$ sampling rate. The analog input voltage range is single-ended and configured to be $5\,\mathrm{V}$. The analogue input has an impedance of $50\,\Omega$ for the purpose of impedance matching. The analogue-to-digital conversion is based on pipelining. A sample takes six clock cycles from the moment it was sampled until it appears at the digital output. This ADC is used for electrical measurements and thus connects to the readout-board via a coaxial SMA cable with a typical impedance of $50\,\Omega$.

The second ADC is an AD9446. As it serves in the optical system, its resolution and sampling rate are critical for the performance of the OCT system. A more high-end ADC is favourable. The AD9446 offers 16 bits in resolution, up to 100MSps sampling rate and better performance in terms of signal-to-noise ratio and dynamic range. Its inputs and outputs are differential. A transformer couples the signal from the photodetector to the input of the ADC.

The specifications of both ADCs are summarized in Table 4.2.

	ADS804	AD9446	
Sampling frequency	10	100	MSps
Resolution	12	16	bits
Input voltage range	0-5	4	V_{p-p}
Pipeline length	6	13	clock cycles

Table 4.2. Specifications of the A-to-D converters used on the data-acquisition-board

Besides the two analog inputs, a 6-pin header on the data-acquisition-board offers four digital input/outputs and two grounds. Two of those are used as digital outputs to the readout-board, the HOLD and SWITCH signals.

4.4.2 Digital electronics design

By 'digital electronics', the part of the electronics is meant that deals with logical signals rather than analogue signals. In this case, the digital electronics cover all the electronics that comes after the ADCs in the signal path, up until the USB controller that connects to the PC. All digital electronics are described in VHSIC Hardware Description Language (VHDL) and loaded into the FPGA via the USB controller.

The electrical signals and the optical signals are treated separately inside the FPGA. Both systems operate independently, but they are controlled by the same triggers from MATLAB®. This keeps all signals synchronised. The digital electronics design knows two modes. In the measuring mode, all data is gathered for a few periods of the excitation signal. The data is stored temporarily in First-In-First-Out (FIFO) registers. In the second mode, the data from the FIFO registers is uploaded to the PC via USB. The starting and switching between modes is regulated by triggers from MATLAB®.

Acquisition of electrical data

The signal path for electrical data starts at the ADC and goes directly to two FIFO registers, one for voltage data and one for current data. During the uploading mode, the FIFO registers are written to the USB controller.

The data flow is controlled by the Finite State Machine (FSM), depicted in Figure 4.7. After start-up, the FSM is in the state 'idle'. The left-hand side of the 'idle'-state represents the upload mode, the right-hand side is the measuring mode. The FSM waits in the 'idle'-state until it receives a trigger from MATLAB®. In general, the first trigger is the command 'SAMPLE' to start the sampling sequence. After the sampling sequence, i.e. when a predefined number of samples is taken, the FSM returns to 'idle'. The next step is the upload mode. When MATLAB® is ready to receive the data, the FSM is commanded to send. After receiving all the data, the FSM is put back into 'idle' by MATLAB®. While the FSM is in the state 'send_data', it is insensitive to both the internal sample triggering and the SAMPLE command from MATLAB®. In other words, the FIFO registers are 'write-only' in measuring mode and 'read-only' in upload mode.
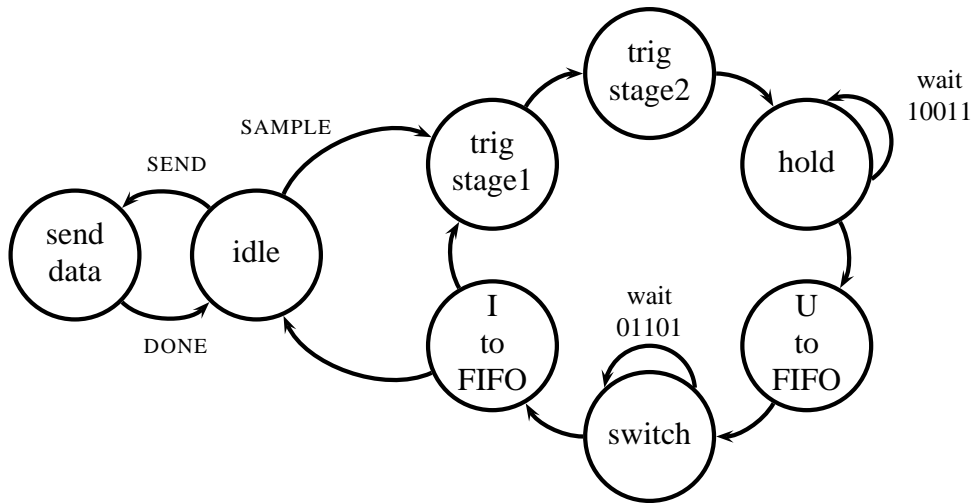

Figure 4.7. Finite State Machine for data acquisition of electrical signals

In measuring mode, the system takes a sample at every rising edge of the signal 'sample_trigger' until a predefined number of samples is taken. The state 'trig_stage1' waits for this signal to be low, state 'trig_stage2' is passed when the signal becomes high. Hence, the combination of both makes the FSM wait for a rising edge in the signal 'sample_trigger'. The state 'hold' makes the signal HOLD to the readout-board low and waits for an appropriate amount of time before continuing to the next state. The voltage data is now written to a FIFO register. At this point, the voltage signal is sampled and stored. The SWITCH-signal is now made low to select the current signal instead of the voltage signal. After the proper delay, also this value is stored in the second FIFO register. When the number of samples to be taken is met, the FSM returns to 'idle'. If not, another sample is taken by skipping directly to 'trig_stage1'.

However, there are a few issues that have to be solved to guarantee the validity of the stored data. The FSM described above, together with the solutions to these issues, is developed into an implementation in VHDL. The simplified VHDL design is shown in Figure 4.8. The issues are mentioned below.
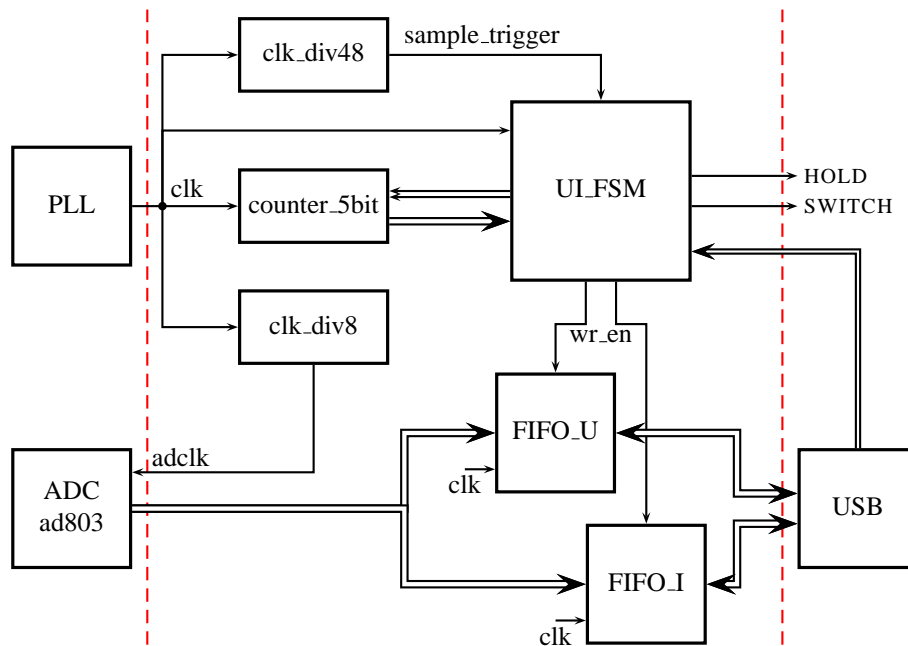
Figure 4.8. Simplified VHDL design of the acquisition system for electrical data

1. The excitation frequency is not fixed. The FIFO registers however have a fixed size.

2. There is a propagation delay in the readout electronics. After applying the HOLD and SWITCH signals, it takes a certain amount of time before the input of the ADC is stable.

3. Both voltage and current data are in the same data stream coming from the ADC

4. The pipeline of the ads804 gives a delay of six clock cycles

To address the first issue, the clock frequency is made flexible. A USB-enabled PLL sets the clock frequency in such a way that 'sample_trigger' has a frequency hundred times faster than the excitation frequency. Doing so, every excitation period is sampled one hundred times at any excitation frequency. Due to the clock divider 'clk_div48', the rest of the blocks runs at a frequency 48 times higher. This gives room for a FSM with a sampling sequence of 48 states at maximum.

To deal with the propagation delay in the readout-board, the 'hold'- and 'switch'-state have a built-in waiting sequence. Besides controlling the HOLD and SWITCH signals, the states also start a counter, the block 'counter_5bit'. The count is fed back to the FSM. Depending on the count, the states decide whether to wait another clock cycle, or to advance to the next state. For a sampling rate of $500\,\text{kSps}$, the clock frequency is $24\,\text{MHz}$. The 'hold'-state waits for 19 clock pulses, which is $800\,\text{ns}$. The 'switch'-state waits 13 clock pulses, $540\,\text{ns}$. The counter is reset to zero in the states following the 'hold'- and 'switch'-states.

There is only one data stream coming from the ADC. The data content depends on the position of the switch on the readout-board. The FIFO registers both have the same data input and the same clock signal. The FSM differentiates between the two by means of the write-enable 'wr_en'. The state 'U_to_FIFO' in Figure 4.7 is implemented by making the write-enable of FIFO_U high, which allows the FIFO register to write one sample into its memory. The write-enable of the other register is low, and thus the register ignores this particular sample. The state 'I_to_FIFO' works similar but selects FIFO_I.

The issue with the ADC pipeline is that it introduces a additional delay of six clock cycles. The FSM would have to wait in total twelve clock cycles more. This leaves only a few clock cycles for other tasks and reduces the flexibility of the system. A way to solve this is to exploit the advantages of the pipeline. By applying a clock signal 'adclk' to the ADC that has a frequency six times higher than 'sample_trigger',

the delay introduced by the pipeline of the ADC is exactly one sample period. The sample data written to the FIFO registers are thus the samples taken in the previous sampling sequence. The validity of data is now secured for all samples, except for the first sample. This is solved by discarding the first sample data in MATLAB®. The clock divider 'clk_div8' provides the clock frequency for the ADC. A disadvantage of this approach is that the resolution to cope with the delays on the readout-board is reduced from $\frac{1}{48}$ to $\frac{1}{6}$ of a clock cycle. This limits the maximum sampling frequency to $500\,\text{kSps}$.

Eventually, when the predefined number of samples are taken, the FIFO registers contain all this data. The USB controller is able to read out the FIFO registers and makes them available in MATLAB® as vectors with decimal representations of the bit-values of the ADC.

Figure 4.8 shows a simplified implementation in VHDL. In the complete design, all blocks are equipped with a reset and there is an output buffer added between the clock signal 'adclk' and the ADC.

Acquisition of optical data

The signal path for optical data is more straight-forward. The functionality of the digital electronics in the case of optical data is not only to store the data samples, but also to perform Amplitude Modulation (AM) demodulation. Information about the group velocity v_g as described in equation 2.9 is in the envelope of the optical signal. The optical signal is thus sampled, then AM demodulated and then stored into a FIFO register. The task of the FSM here is only to start and stop the sampling according to the triggers from MATLAB®. The simplified VHDL design is depicted in Figure 4.9.
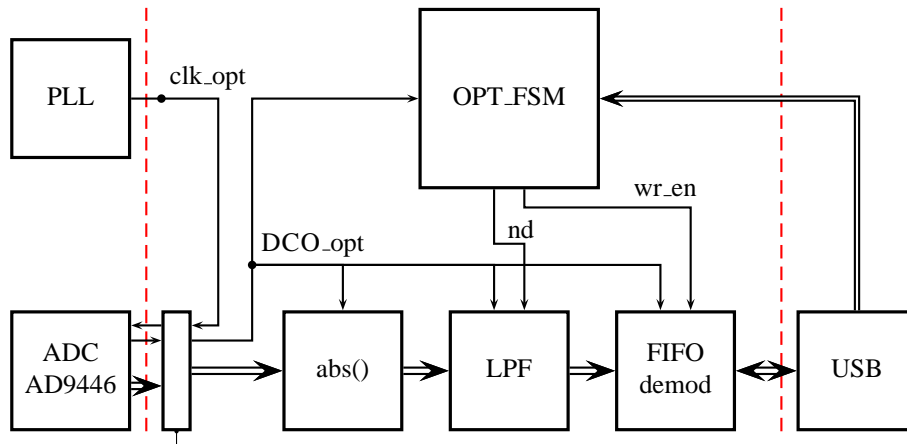

Figure 4.9. Simplified VHDL design of the acquisition system for optical data

The PLL generates the clock signal such that 1000 samples are taken for every excitation period. The clock signal is fed directly to the ADC. The clock signal for the rest of the design is 'DCO_opt'. This is the same clock signal as the one coming from the PLL, but it has the same phase delay as the samples taken by the ADC. The phase delay between 'clk_opt' and 'DCO_opt' becomes relevant at high sampling frequencies. The samples from the ADC are thus in phase with 'DCO_opt'.

Any signals between the FPGA and the ADC have to be translated from differential signals to single-ended and vice versa. The block in Figure 4.9 that interfaces all the signals coming from and going to the AD9446 contains a number of buffers that provide this functionality.

Once the sample data is single-ended, it can be demodulated. The ground level of the signal is exactly in the middle of the digital range. Therefore it is fed to the block 'abs()' that calculates the absolute value of the optical signal and subtracts this digital offset from the sample data. Thereafter, the absolute values are filtered by a digital low-pass Finite Impulse Response (FIR) filter and stored in the FIFO register.

The FIR filter has a normalised cut-off frequency at $\frac{\pi}{10}$. The filter has 150 orders, which results in the filter characteristic shown in Figure 4.10. As the optical signal is low-pass filtered, the signal no longer contains high-frequency components. The data can be compressed by decimating the output of the filter, a built-in

feature of the block 'LPF'. The decimation factor used is four. The output sample frequency of the block 'LPF' is four times lower than the input frequency.
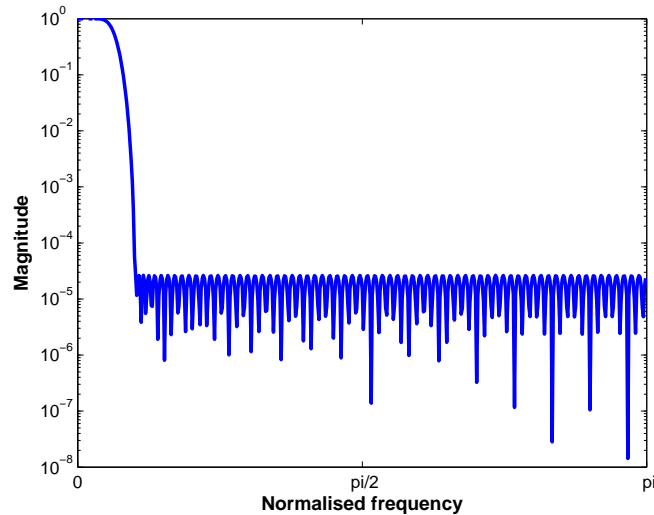

Figure 4.10. Transfer function of the FIR low-pass filter with 150 orders

To verify the AM demodulation, the data from 'FIFO_demod' is compared to the raw optical data. This comparison is shown in Figure 4.11. The figure shows an interference pattern in blue and the AM demodulated signal in red. The maxima in the interference pattern represent a reflective object within the scanning range of the measurement setup. In the measurement setup, the reflective object is a mirror. The mirror is detected twice, once during a falling flank for $t < 5\,\mathrm{ms}$ and once for a rising flank of the excitation signal.

The shape of an interference pattern is determined by the source and the chromatic dispersion. Ideally, the shape would look similar to the right-hand side of Figure 2.1. Due to dispersion, the interference pattern is smeared out. The better the chromatic dispersion compensation, the narrower the shape and thus the better the resolution.

As Figure 4.11 shows, both the shape and the location of the maxima are well captured by the AM demodulated signal. The amplitude is of minor interest for the measurements in chapter 5, only the signal-to-noise ratio (SNR) should be high enough to reliably detect the maxima. In contrary, for OCT the amplitude is a matter of interest and the SNR should be high to be able to detect weak reflections.

4.4.3 MATLAB scripting

MATLAB® has the top-level control of the measuring process. It controls the excitation electronics, the position of the mirror and communicates with the FSMs and the PLL. Its tasks can be divided into three categories, being initialisation, measurement control and visualisation. The categories are discussed in the following sections.

Initialisation of the measurement setup

The initialisation starts with the definition of all the measurement parameters. The parameters specify which TODL is used at which excitation frequency and how many excitation periods have to be analysed. This results in the sampling parameters, such as the number of samples to be taken and the sampling frequencies. The initial position of the mirror is determined, together with the expected scanning range and the number of mirror positions to be analysed.
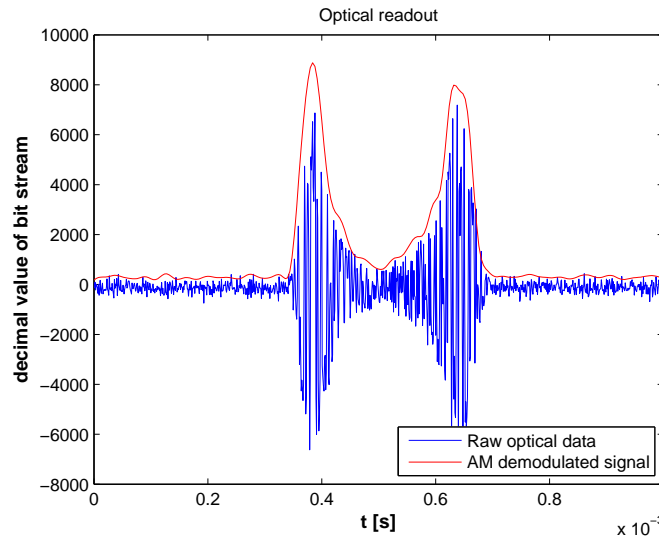
Figure 4.11. AM demodulation of the optical signal

After definition of the necessary parameters, all the devices under control by MATLAB$^{\circledR}$ are initialised. The synthesized VHDL design is loaded into the FPGA and the output frequencies of the PLL are set. The mirror is moved to its initial position. Finally, the voltage excitation waveform is loaded from a mat-file and the TODL is pre-heated by switching on the excitation signal for 5 seconds. Without preheating, the first measurements show abnormal behaviour that is believed to be caused by the TODL. The last step is the allocation of PC memory for the measurement data. The measurement setup is now ready to measure.

Measurement control

In the measurement parameters, a number of mirror positions are defined. For every position, a measurement has to be done. A single measurement is described below:

1. Move mirror

2. Start excitation signal

3. Trigger sampling process by sending the command SAMPLE to the FSMs

4. Read out the three FIFO registers

5. Pre-process data from FIFO registers

6. Find the desired number of excitation periods

7. Store the acquired data

Two of the steps require further explanation. Firstly, the pre-processing mentioned in step 5. The data that is read out from the FIFO registers is a decimal representation of the bit-values of the two ADCs. For the electrical signals, these decimal values are translated to the voltages measured by the ads804 ADC. The offset and scaling factor used are calibrated using a Tektronix TDS2014B oscilloscope. The decimal values that represent the optical signal are scaled by a factor 2^{12}. Doing so, the optical signal has a similar range as the electrical signals, which is convenient for visualisation purposes.

Secondly, finding the desired number of excitation periods is done by a similar manner as the triggering of an oscilloscope. The script analyses one of the signals, the voltage signal, and stores the time instants where

a certain threshold value is crossed. The period between two of these time instants is thus one excitation period. The desired number of periods is selected from the data. The corresponding excitation periods for the current signal and the optical signal are deducted from the same time instants.

Optionally, the measurement process can be repeated several times to average out uncorrelated measurement errors.

Visualisation of the acquired data

During the measurement process, real-time visualisation of the acquired data makes it possible to check whether the measurement process is going well. Every mirror positions results in a measurement as shown in Figure 4.12. The figure shows the voltage, the current and the optical signal of the most recent measurement data. The figure shows three periods, hence six line scans.
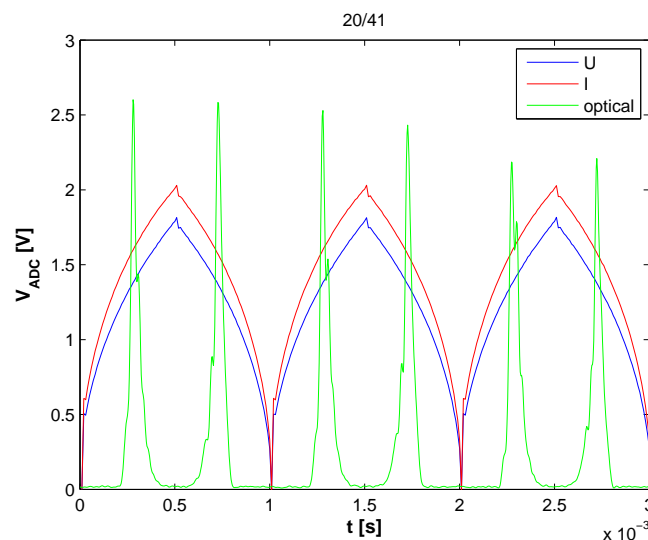

Figure 4.12. Scan of a mirror positioned in the middle of the scanning range with a TODLwith a width of $88\,\mu$m at an excitation frequency of $1\,$kHz.

After the measurement process, MATLAB$^{\circledR}$ shows all the optical data in an intensity plot such as Figure 4.13. Any errors in acquisition or in triggering can easily be spotted here. MATLAB$^{\circledR}$ also shows the resistance over one excitation period, averaged over all the excitation periods measured.

4.5 Low-coherent light source

The low-coherent light source used is a SuperLuminescent Diode (SLD). This kind of light source is a compromise between a Light Emitting Diode (LED) and a Laser Diode (LD). A SLD can be seen as a LED with a built-in waveguide. The spontaneously emitted light is captured in the waveguide and therefore exploits the optical amplification that is common to LDs. On the other hand, this optical amplification goes hand in hand with narrowing of the optical bandwidth. This explains the narrow bandwidth and the high efficiency of a LD. In a SLD, the spontaneously emitted light passes the waveguide only once to retain a wide bandwidth, at the cost of efficiency.

Due to the waveguide, the generated light is confined into a single direction. This significantly enhances the coupling efficiency into a single-mode optical fibre, compared to a LED.

The optical source is a SLD from Exalos, type EXS13G2-2311. In table 4.3, the specifications of interest are listed. Substitution of these values in equation 2.6 results in the theoretical axial resolution of the
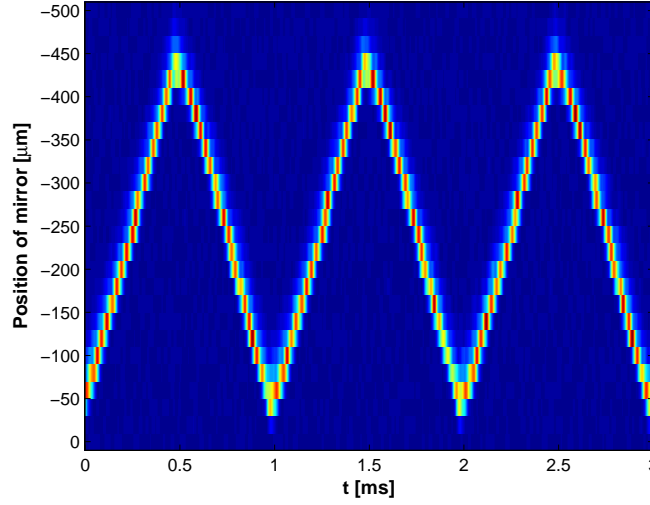
Figure 4.13. Optical data acquired for a TODLwith a width of $88\,\mu$m at an excitation frequency of $1\,$kHz and double reflection

system. Equation 2.6 is repeated here as equation 4.1. The axial resolution for the EXS13G2-2311 is $13.6\,$nm. Whether or not this resolution can be obtained in practice depends on the chromatic dispersion, which will be dealt with in section 4.6.

Centre wavelength λ_0	$1300\,$nm
Bandwidth $\Delta\lambda$	$55\,$nm
Max. power P	$20\,$mW

Table 4.3. SLED specifications (EXS13G2-2311)

$$\Delta z = \frac{2\ln 2}{\pi}\left(\frac{\lambda_0^2}{\Delta\lambda}\right) = \frac{2\ln 2}{\pi}\left(\frac{(1300\,\text{nm})^2}{55\,\text{nm}}\right) \approx 13.6\,\text{nm} \qquad (4.1)$$

4.6   Chromatic dispersion compensation

Compensation of chromatic dispersion implies a wavelength-dependent optical network that cancels the difference in delay between the spectral components of a beam. However, a TD-OCT system makes use of two optical paths. To undo the broadening of the interference pattern caused by chromatic dispersion, equalising the dispersion in both arms suffices.

The most straigth-forward manner to achieve similar delays for every spectral component is to make both the reference arm and the sample arm as similar as possible. The beam in the reference arm travels through the TODL, which consists of silicon. To compensate for the dispersion in the TODL, one can add another piece of silicon in sample arm. The OPL in this piece of silicon should be equal to the OPL in the TODL.

Although most of the OCT system consists of optical fibre, a free-space part is present in the system. A fibre collimator connects the optical fibre part to the free-space optical part. It is placed on a linear stage in such a way that the OPL can be tuned to match the other arm. The fibre collimator produces a collimated gaussian beam with a diameter of $5\,$mm. A block of silicon can be placed in line with this beam, as shown in Figure 4.14. The black rectangle represents a top view of the silicon block, the centre of the beam is depicted in red. By placing the silicon block under an angle, one can differentiate between the multiple

reflections. Reflection losses can be minimised by selectively adding a reflective layer where total internal reflection is favourable.
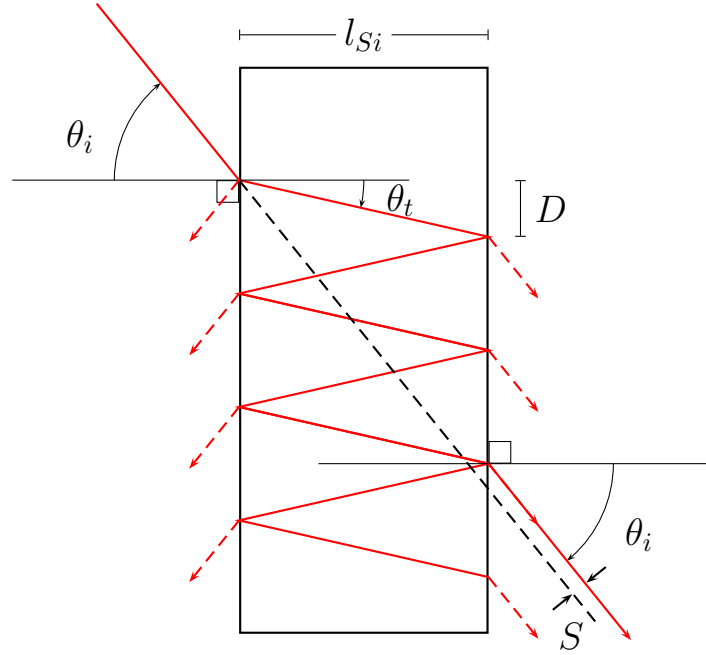

Figure 4.14. Illustration of the dispersion compensation block with a number of internal reflections at an incident angle of 51.1 °

To be able to differentiate between reflections, the incident angle must be chosen in such a way that the lateral displacement of the beam D is bigger than the radius of the beam r_{beam}. The Optical Path Length between the two sides of the silicon should be equal to the length of the TODL, l_{TODL}. These two values determine the length of the silicon block l_{Si} through equation 4.2.

$$l_{Si} = \sqrt{l_{TODL}^2 - r_{beam}^2} \tag{4.2}$$

For proper alignment of the block, two values are of interest. Firstly, the lateral displacement of the beam D, i.e. the spot along the side of the silicon block where a certain reflection will exit the block. When evaluating the displacement for every reflection, one knows where to apply a reflective layer. Secondly, the lateral shift of the beam S. The lateral shift is of importance for alignment. Both are a function of the incident angle θ_i.

Part of the beam will exit the block after a number of reflections N at a distance ND from the point of incidence. On the left side in Figure 4.14 after an even number of reflections, on the right side for an odd number of reflections. The lateral displacement D can be calculated from equation 4.3. The parameters n_{air} and n_{Si} correspond to the refractive indices of air and silicon. As an example, Figure 4.14 shows the transmitted beam after five reflections in more detail.

$$D = l_{Si} \tan \theta_t = l_{Si} \left(\frac{\frac{n_{air}}{n_{Si}} \sin \theta_i}{\sqrt{1 - \left(\frac{n_{air}}{n_{Si}} \sin \theta_i \right)^2}} \right) \tag{4.3}$$

The beam shift is directly related to the beam displacement, but now with respect to the incident beam instead of the point of incidence. This value represents the lateral distance between the transmitting end and the receiving end. The beam shift is given by equation 4.4.

$$S = (ND - l_{Si} \tan \theta_i) \cdot \cos \theta_i \tag{4.4}$$

The angle of incidence calculated for a beam diameter of $5\,\text{mm}$ is $51.1\,°$. At this angle, the losses for every reflection are high. The silicon bar has to be coated with a reflective layer to reduce losses. Other options are the use of an anti-reflective layer and a smaller collimated beam. The beam shift for a single reflection at this angle of incidence is $-7\,\text{mm}$.

4.7   Photodetector

The photodetector used is a PDB150C from Thorlabs. This is a balanced photodetector, which provides differential optical measurement for increased SNR compared to a single detector. It has a built-in transimpedance amplifier with switchable gain and a bandwidth depending on the gain setting. In the characterisation setup, a gain of $10^5\,\text{V/A}$ is used, which corresponds to a bandwidth of $5\,\text{MHz}$.

The SNR of the system can be calculated from equation 2.8, under the assumption that the photodetector is the main noise source. Equation 2.8 is repeated here in equation 4.5 for convenience.

$$SNR = 10 \log \left(\frac{\eta P_{opt}}{2h v NEB} \right) \tag{4.5}$$

Parameters h and v relate to the energy of a photon, with h Planck's constant and v the velocity of the photon. The NEB and the quantum efficiency η are properties of the photodetector. Both can be extracted from the Operation Manual [26]. The NEB is equivalent to the bandwidth of the detector, $5\,\text{MHz}$. The quantum efficiency is given as the responsivity R of the detector. Equation 4.6 converts the responsivity into the quantum efficiency that is used in 4.5. The responsivity of the detector at $1300\,\text{nm}$ is $0.95\,\text{A/W}$, which corresponds to a quantum efficiency of 0.91.

$$\eta = \frac{R}{q} \cdot \frac{hc}{\lambda_0} \approx 0.91 \tag{4.6}$$

The optical power P_{opt} that illuminates the photodetector is equal to output power of the low-coherent source after taking into account the losses in the optical system. These losses include transmission- and reflection losses. Hence, the optical power P_{opt} is a function of the number of reflections used to obtain the scan range.

4.8   Scanning mirror

As a reference object, a mirror is used. The mirror is placed on a motorized linear stage by Thorlabs. The steppermotor is driven by a steppermotor controller from Standa, the 8SMC1-USBh. This controller is connected to a PC via USB. The drivers for the PC are compatible with MATLAB®.

The rotation of the steppermotor is translated to a displacement. The displacement of one step is $1\,\mu\text{m}$. As the theoretical resolution of the measurement setup is much higher, the resolution of the motorized linear stage suffices. The steppermotor controller allows an input range from -2^{16} to 2^{16}. The range of the mirror is thus $\pm 2.5\,\text{cm}$. The expected scanning range of the measurement setup is $200\,\mu\text{m}$. At most, with five reflections, the scanning range will be $1\,\text{mm}$. For the measurements of chapter 5, the scanning mirror covers a range of $3\,00 - 400\,\mu\text{m}$ with steps of $10\,\mu\text{m}$.

Chapter 5

Verification of the TODL models

For verification of the TODL models, the combination of the model and the TODL have to be tested to what extent the variation in effective optical path length matches the ideal situation as defined in section 3.8.1. The parameters to evaluate are introduced and explained in section 5.1. Both models are compared to each other in section 5.2. Section 5.3 compares the acquired optical measurements to the electrical signals analysed. Sections 5.4 and 5.5 evaluate the non-linear model for a variety of frequencies and ambient temperatures respectively. Finally, the findings are discussed in section 5.7.

5.1 Data analysis

The raw data coming from the measurement setup has to be analysed to extract the parameters that are important for verification of the model. The goal is to achieve linearity of the delay variation in the TODL. The region where linearity is required is defined by the scanning range. The scanning range depends on the thermal behaviour of the TODL and is therefore unknown beforehand. The scanning range can be extracted from the optical data as described in section 5.1.1. In order to investigate the linearity, a measure has to be defined that represents the extent to which the variation of the effective optical path length is linear. This is discussed in section 5.1.2. The temperature of the TODL as a function of time offers a second view on the accuracy of the model. The temperature of the TODL can be extracted from the electrical data. This is explained in section 5.1.3.

The figures in this section are generated from measurements performed on a TODL with a width of $88\,\mu\mathrm{m}$ at an excitation frequency of $1\,\mathrm{kHz}$.

5.1.1 Scanning range

To find the scanning range, one has to analyse the optical data. Apart from noise, an optical signal only exists when interference occurs and interference only occurs within the scanning range. The scanning range is found by taking the FWHM range of the optical power.

Figure 5.1 shows the average optical power received by the photodetector plotted as a function of the mirror position. The line corresponding to half of the maximum optical power is depicted horizontally in black. The vertical red lines mark the mirror position closest to half the maximum. The scanning range is defined as the distance between the two marked mirror positions.

5.1.2 Linearity and error

To investigate the linearity, the peaks in the interference pattern have to be compared with the positions of the mirror. A peak in the interference pattern is caused by a reflection of the mirror. One line scan is taken
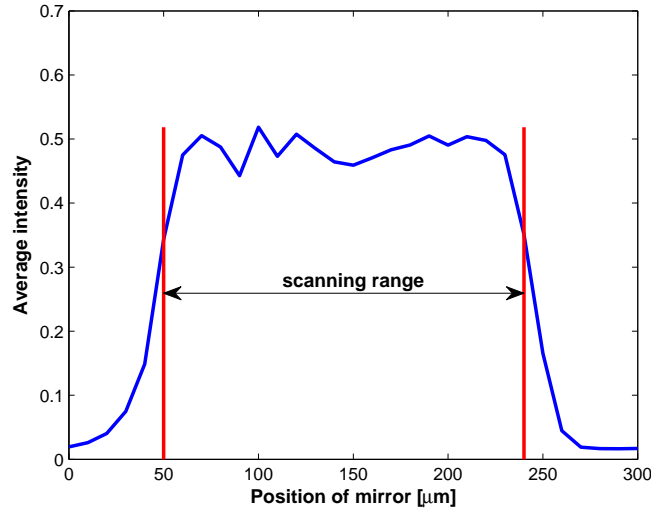
Figure 5.1. Full-Width-at-Half-Maximum scanning range as calculated by MATLAB®

in half of the excitation period. The scanning range can thus be mapped onto the time domain covered by half of the excitation period. The time instant at which the peak is detected relative to this time domain translates into a measured mirror position relative to the detected scanning range.

The physical mirror position determined by the steppermotor is now plotted against the position that is deducted from the optical signal. Figure 5.2 shows the rising flank of the waveform as 'up' and the falling flank as 'down'. For comparison of the two flanks, the falling flank is flipped along the x-axis. Ideally, the measured position and the mirror position should be equal for every position. The ideal curve is shown as a black line. Due to the flipping, point symmetry of the two curves with respect to the middle of the scanning range implies similar behaviour of the line scans 'up' and 'down'.

To reduce the errors induced by the measurement setup, multiple measurements are carried out. Each line scan contains five periods of the excitation waveform. The peaks detected for each period are averaged along the five periods. On top of that, the line scanning process is repeated such that the scanning range is covered five times. Unlike the peaks, the data of each line scanning process is stored separately. The curves in Figure 5.2 show the mean for each mirror position as a coloured square. The standard deviation is denoted as a range in the vertical direction.

The error is defined as the difference between the ideal curve and the measured curve. For a qualitative analysis, the error is put into a bar graph, Figure 5.3. Here, both flanks are plotted chronologically from left to right. To compare the response of the TODL in a more objective way, the R^2-value is calculated. Given the linearity of the ideal curve, the R^2-value is a measure for the percentage of the measurement data that can be explained by a linear approximation. Hence, the value $(1 - R^2)$ is a measure for the non-linearity of the measurement data. In MATLAB®, the function `regstats` is used to calculate R^2 with the ideal curve and the measured curve as its input parameters.

5.1.3 Temperature

The measurement data also comprises the electrical signals applied during excitation. By dividing the voltage signal by the current signal for every time instant, the instantaneous resistance of the platinum heater is calculated. The resistance of platinum is a function of temperature, as stated in equation 3.1. The instantaneous temperature of the membrane close the waveguide can be deducted by reversing equation 3.1 and substitution of the calculated instantaneous resistance.

As the resistance measurement is prone to errors due to both phase difference and noise, the resistance is
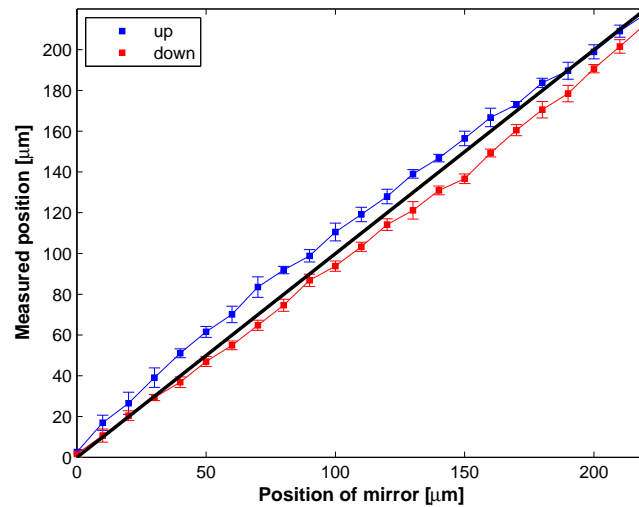
Figure 5.2. Measured position of the mirror versus the position according to the steppermotor at an excitation frequency of 1 kHz
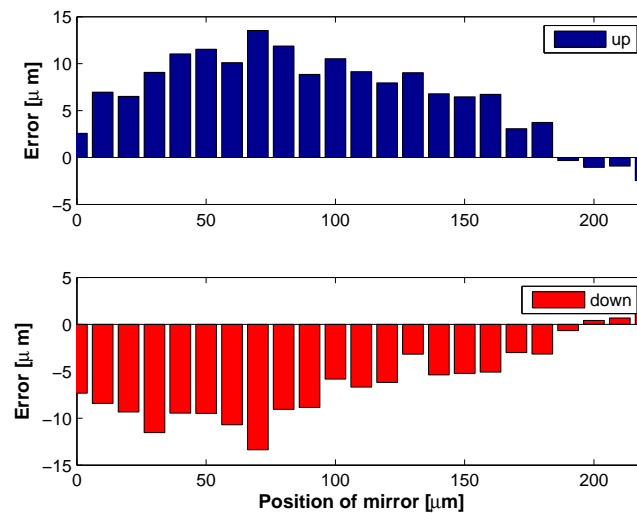

Figure 5.3. Bar graph of the error between ideal curve and the measured positions at an excitation frequency of 1 kHz

averaged over all measured periods of the measurement process. The excitation waveform does not change during the measurement process and thus the resistance should be similar for every period. Inspection of the measurement data for voltage and current show that the measured waveforms remain constant over the measuring period. The main source of variation is due to triggering on a steep part of the waveform.

5.1.4 Peak power

The peak power is calculated similar to the resistance. As the excitation waveform does not change, the voltage and the current are similar, unless the resistance changes. The voltage and current are averaged over all the excitation periods measured. The power waveform follows from multiplying the voltage and the current. The peak power is the maximum of this power waveform.

5.2   Comparison between linear and non-linear model

The goal of both models is to produce a variation in effective optical path length that equals Figure 3.14. This figure is characterised by two requirements. The scanning range has to be $200\,\mu$m and transition between the ends of the scanning range has to be linear. The linear model and the non-linear model are compared at an excitation frequency of $1\,$kHz for a TODL of $88\,\mu$m wide. The measured resistance R_0 was $71.9\,\Omega$.

Figures 5.4 and 5.5 show the scanning range and the linearity for the linear model and the non-linear model respectively. The excitation waveforms for both models are shown in Figure 3.16. The peak voltage of the linear model is considerably higher than for the non-linear model. A higher scanning range is thus expected for the linear model.

The FWHM scanning range for the linear model is $320\,\mu$m, whereas the non-linear model comes to a scanning range of $200\,\mu$m. This confirms that the thermal conductivity cannot be regarded a constant. Furthermore, according to the optical measurements, the non-linear relation for thermal conductivity is accurate for an excitation frequency of $1\,$kHz.

In terms of linearity, the linear model performs poorly. Both line scans, up and down, are bended in the same direction compared to the ideal curve. This means that the 'up'-scan is very different from the 'down'-scan. This is an unwanted behaviour. On the contrary, the non-linear model shows the point-symmetry, implying that the heating up and cooling down happens in a similar fashion. This shows even better in the errors from Figure 5.3, which is also taken at $1\,$kHz. The shape of the error suggests that the membrane is behaving more slowly than expected. The membrane is not keeping up with the discontinuities in the waveform. This manifests itself as 'hysteresis' in the optical behaviour.

The rate of heat flow and therefore the speed of the membrane is characterised by the thermal diffusivity. A slower membrane implicitly states that the thermal diffusivity in the model was chosen too high. This statement is investigated further in section 5.4.
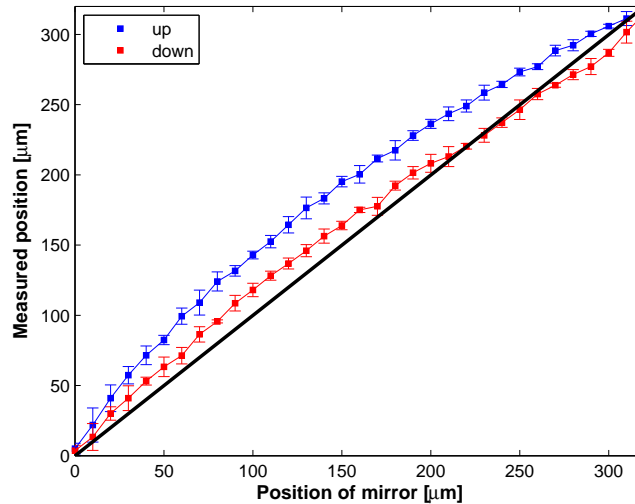

Figure 5.4. Scanning range for linear model for a TODL of $88\,\mu$m at an excitation frequency of $1\,$kHz

The linear model has proved itself not accurate. Both scanning range and waveform are very different from the predictions. It will not be used for further analysis. The non-linear model does its job well in terms of thermal conductivity, although a remark has to be made. The measurements shown in Figure 5.5 are based on a resistance R_0 equal to $71.9\,\Omega$ instead of $80.0\,\Omega$. This explains the difference in scanning range between Figures 5.2 and 5.5. The modeled thermal diffusivity seems on the high side. This can be tested by analysing the frequency behaviour of the membrane, section 5.4.
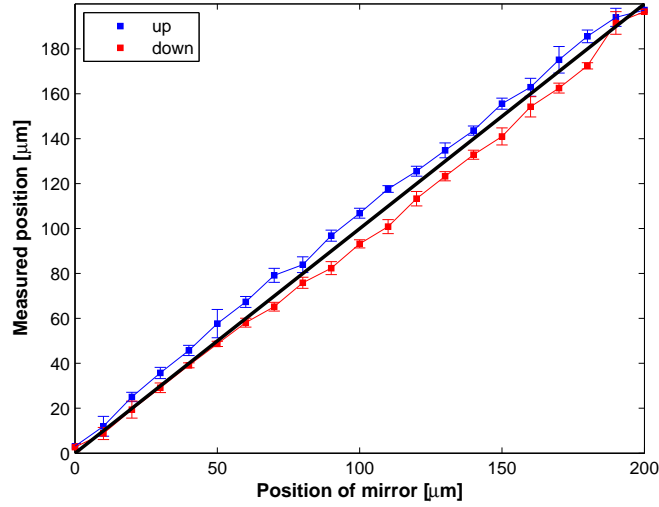
Figure 5.5. Scanning range for non-linear model for a TODL of $88\,\mu$m at an excitation frequency of $1\,\text{kHz}$

5.3 Comparison between temperature and optical measurements

The comparison of the thermal behaviour versus the optical behaviour is meant as a double-check of the modelling done in chapter 3. The relations for thermal conductivity and diffusivity given in chapter 2 are for instance conducted for bulk silicon. The thermo-optic effect is determined for a wavelength of $1523\,\text{nm}$ and is based on phase velocity only. By measuring the temperature of the membrane, an intermediate step is taken which can help to find the origin of deviations between model and measurements.

Figure 5.6 shows the thermal response in one excitation period. The waveform predicted by the non-linear model is shown in red, the measured waveform in blue. The amplitude and the offset of the measurements do not comply to the predicted waveform. Through equation 3.1, both are very sensitive to deviations in R_0. However, this does not fully explain the factor two between the predicted and measured waveforms. The temperature measurements are discussed further in section 5.7.

When the measured waveform is scaled to match the predicted waveform, the green waveform in Figure 5.6, one can compare the two in terms of delay and shape. Measurements show a slight delay, invisible at frequencies below $500\,\text{Hz}$ but distinguishable in Figure 5.6. Another observation to make is that the rising flank matches the predicted waveform after scaling. The falling flank shows a lag. In other words, the heating of the membrane happens roughly according to the model, the cooling down of the membrane is slower than predicted.

Comparing the scaled measurements from Figure 5.6 to the optical signal in Figure 5.7 also shows a lag, but for both the rising flank and the falling flank. The $1 - R^2$-values for the rising and falling flank are $5.1 \cdot 10^{-3}$ and $7.2 \cdot 10^{-3}$ respectively, also suggesting that the falling flank is the worst of the two.

5.4 Frequency behaviour

The TODL model is supposed to be accurate for excitation frequencies up to $5\,\text{kHz}$. Also, the model should be able to take into account the width of the membrane. To verify the frequency behaviour of the non-linear model, a number of excitation frequencies are tested for two membrane widths. With the frequency response of the two membranes at hand, the trade-off between power and speed can be investigated further.

Figure 5.8 shows the frequency behaviour for the scanning range of the combination of the TODL and the pre-emphasis imposed by the non-linear model. Due to the pre-emphasis, the power is not constant for all
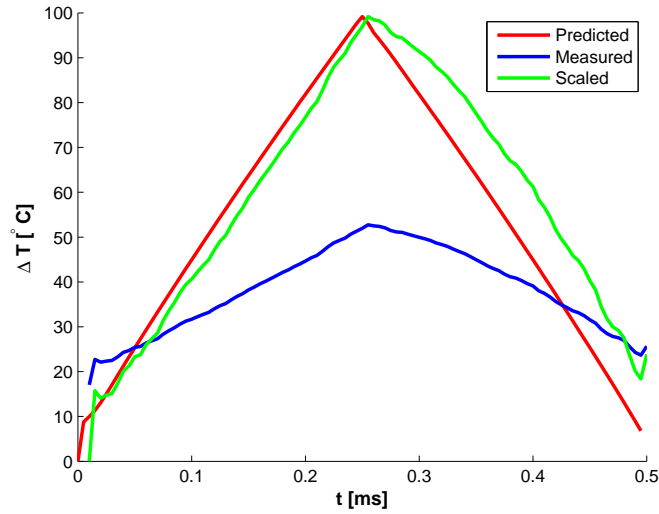
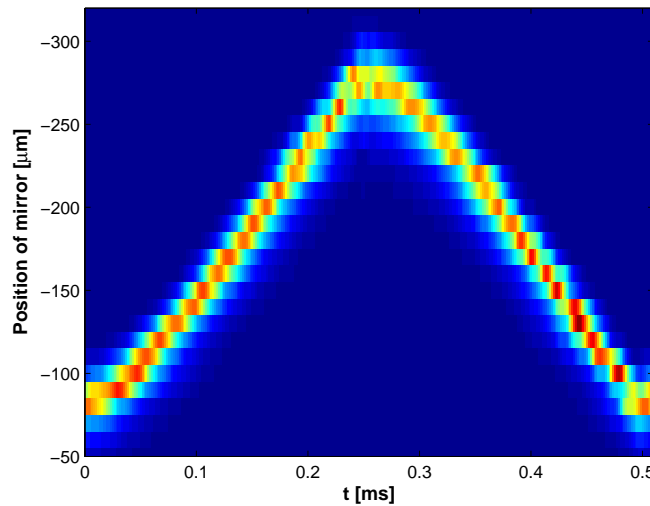**Figure 5.6.** Predicted temperature behaviour compared to the measurements

Figure 5.7. Intensity plot of the optical signal for one excitation period

frequencies. Ideally, both curves would show a flat response at $200\,\mu$m. Instead, both show a decrease in scanning range over frequency. The curve in blue represents the narrow membrane, $88\,\mu$m. In red, its wider counterpart with a width of $118\,\mu$m. The narrow membrane shows a flat region for low frequencies. At moderate frequencies, the scanning range falls off at with slope of $-20\,\mu$m per octave. At frequencies above $4\,$kHz, the slope changes to approximately $-60\,\mu$m per octave. For the wider membrane, the two slopes are $-30\,\mu$m per octave and $-60\,\mu$m per octave. The difference is in the fact that for the wider membrane, the second slope already appears at $2\,$kHz. Hence, both membranes show similar behaviour, except the wider membrane has a lower cut-off frequency.

The second requirements, linearity, also shows a deviation over frequency. The $1 - R^2$-values for both membranes are depicted in Figure 5.9. The non-linearity that is left in the frequency behaviour after compensation with the non-linear model increases exponentially. The higher the frequency, the higher the hysteresis in the optical signal.
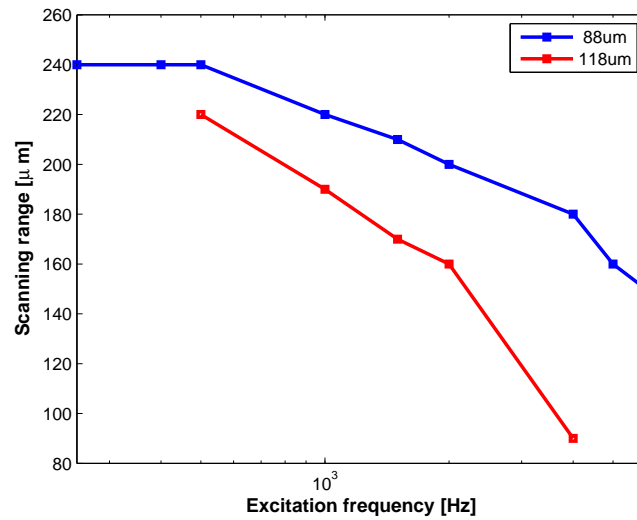
Figure 5.8. Frequency behaviour of the scanning range for two membrane widths

Both the decreasing scanning range and the hysteresis in the optical signal suggest a thermal diffusivity that is in reality lower than in the model. The hysteresis is due to the fact that the membrane heats up and cools down slowlier. Heat is flowing at a lower rate than expected. Eventually, the predicted scanning range can no longer be reached as the voltage excitation waveform is already decreasing before the steady-state behaviour defined by the thermal conductivity has settled.
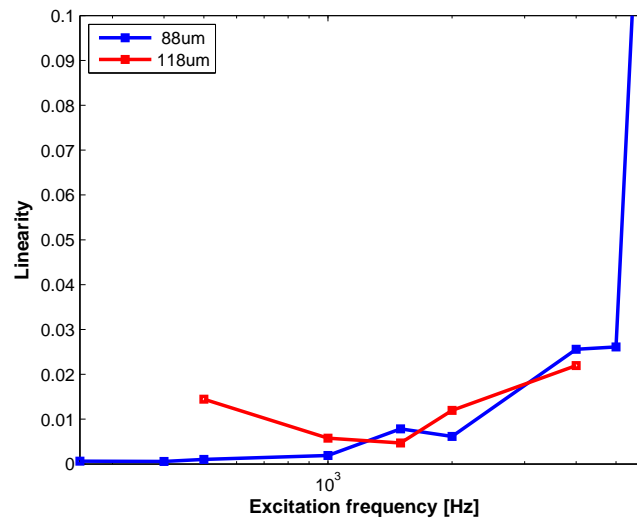

Figure 5.9. Linearity as a function of excitation frequency for two membrane widths

One part of the power-speed trade-off is already discussed. The bandwidth of the wide membrane is lower by a factor two. The peak power used to obtain the scanning range is also lower for the wide membrane. The peak power for the narrow membrane is about $13.3\,\mathrm{W}$, for the wide membrane a peak power of $10.6\,\mathrm{W}$ suffices. Considering the two examples, the product of membrane width and power is roughly constant, as implicitly stated in the model equations. However, this conclusion assumes a scanning range that is equal for low-frequencies, i.e. when the thermal diffusivity has little influence. There are no measurements available with equal scanning range and frequency. To quantify the power-speed trade-off,

more measurements are necessary.

Regarding the frequency behaviour, the non-linear model as described in chapter 3 has a reasonably linear behaviour up to $1 - 2\,\mathrm{kHz}$. For higher frequencies, hysteresis and loss of scanning range render the TODL useless. A plausible solution to these problems lies in the lowering of the thermal diffusivity in the model.

5.5 Variation of ambient temperature

According to the Figure 3.11, the ambient temperature T_0 has a significant influence on the steady-state behaviour of the membrane. To investigate whether the ambient temperature affects the linearity, a number of waveforms are applied assuming different ambient temperatures. The actual ambient temperature is not changed. Figure 5.10 shows the results of the variation of ambient temperature in the model.

As predicted, the scanning range is higher for low ambient temperatures. The model predicts a higher thermal conductivity and compensates for that by increasing the electrical power. There is hardly a relation to find between linearity and ambient temperature. The $1 - R^2$-values vary randomly around a mean value of $2 \cdot 10^{-3}$. Assuming the ideal scanning range, the actual ambient temperature is $35\,^{\circ}\mathrm{C}$. Figure 5.8 shows that the non-linear model results in a scanning range of $240\,\mu\mathrm{m}$. The actual ambient temperature would be $15\,^{\circ}\mathrm{C}$, a value that corresponds to the ambient temperature found by measuring the resistance, Figure 5.6.
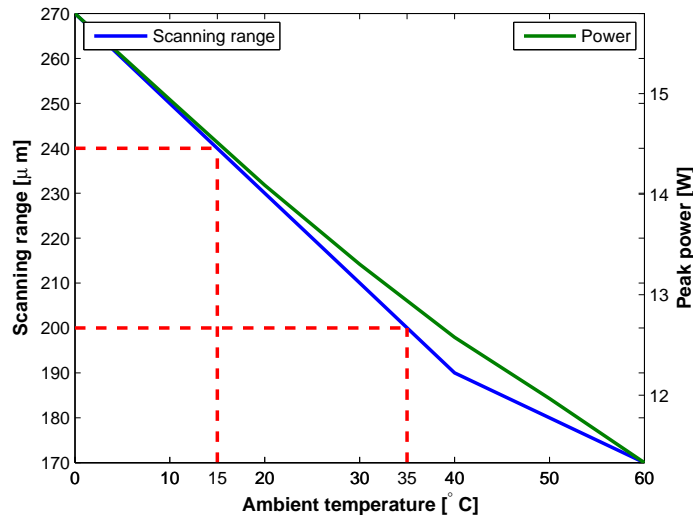

Figure 5.10. Scanning range for non-linear model with assuming a variation of ambient temperature

5.6 TODL response with lowered thermal diffusivity

The findings in the previous sections make it plausible that the thermal diffusivity is in reality lower than literature suggests. To test this assertion, the thermal diffusivity in the non-linear model is scaled down. The proportionality to $T^{-1.8}$ from literature is not altered. In order to fulfill the requirements stated in Table 3.1, the lower thermal diffusivity is put to the test at an excitation frequency of $5\,\mathrm{kHz}$. A few factors are tried, with a factor of 0.4 the most succesful attempt. Lower factors run into problems due to limitations of the iteration process. A startup effect gives a large error at $t = 0$, which keeps the iteration process from converging.

The non-linear model comes up with the waveform that is depicted in Figure 5.11. The optical response of the TODL is given in Figure 5.12. With the proposed scaling of the thermal diffusivity, the scanning

range is increased to $200\,\mu$m compared to $160\,\mu$m for the value from literature. The error is depicted in Figure 5.13. Comparing this figure to Figure 5.3, the non-linear model with corrected thermal diffusivity at $5\,$kHz performs better than the uncorrected non-linear model at $1\,$kHz. Another remark that has to be made, is that the shape of the error is similar to the difference between predicted and measured temperature as shown in Figure 5.6.
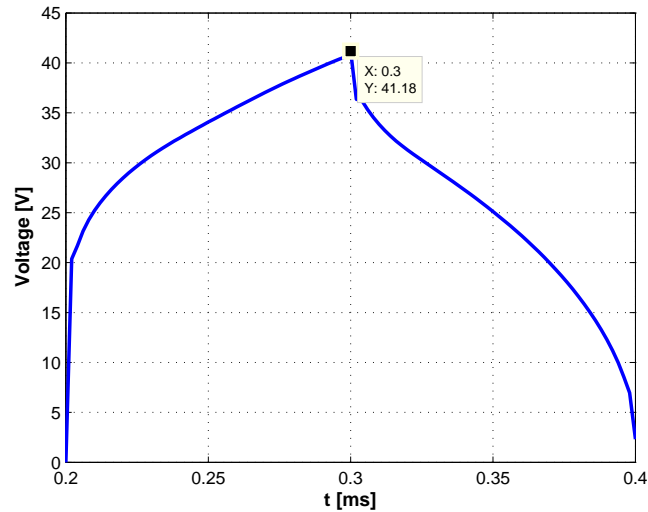

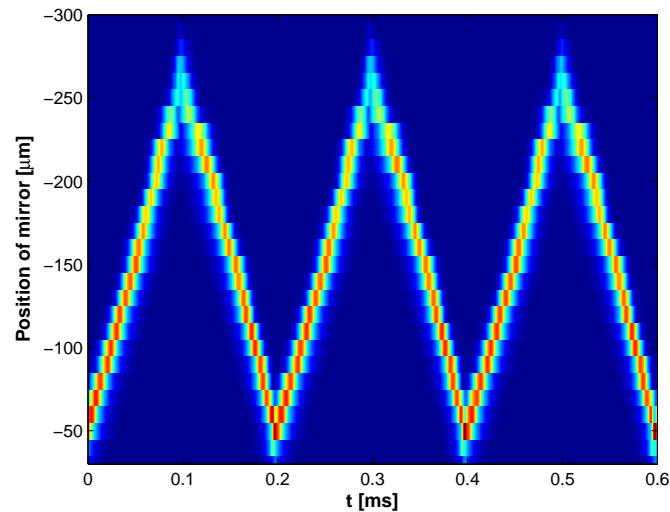**Figure 5.11.** Excitation waveform for a 88 μm wide TODL at 5 kHz (10 kHz line scanning rate)

Figure 5.12. TODL response for an excitation frequency of 5 kHz

5.7 Discussion

Two values are measured for the resistance of the TODL at room temperature, R_0. For the TODL with a width of $88\,\mu$m, R_0 was measured $80.0\,\Omega$ when disconnected from all electronics. When connected to the readout-board with all power supplies switched off, this value dropped to $71.9\,\Omega$. The first value results in
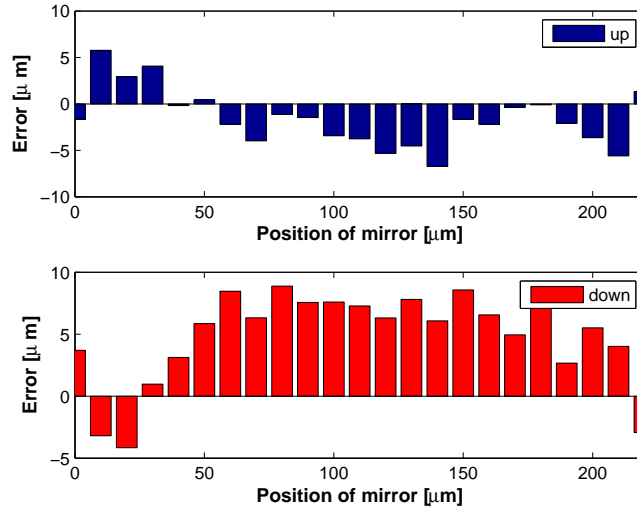
Figure 5.13. Error in micrometers for a 88 μm wide TODL at 5 kHz

a scanning range that is slightly higher, 240 μm instead of 200 μm. The measured value for the ambient temperature T_0 corresponds to the value deducted from optical measurements in section 5.5, 15 °C. Using the other value, the scanning range is equal to 200 μm, but performing the calculations for temperature suggests an ambient temperature of 65 °C. If the temperature of the bulk silicon would be this high, the aluminium bracket would at least be warm. As this is not the case, the first scenario is more likely. The low-frequency scanning range is determined by the thermal conductivity. In order to optimize the non-linear model, the thermal conductivity has to be lowered a bit too. This observation is supported by theory, as the thermal conductivity is a function of the thermal diffusivity by definition (eq. 2.16).

The amplitude of the temperature measurements deviate substantially from the predicted temperature wave-form. An explanation would be that a significant part of the electrical power is lost elsewhere. That can be in the parasitic resistances of the heater, by convection and radiation. Also, the layer of Silicon-nitride might alter the thermal behaviour, although its thermal conductivity is a factor five lower than for crystalline silicon. Literature suggests that the thermal conductivity changes in a similar manner as the thermal diffusivity. The optical measurements however show that the scanning range is close to the predicted values. The reduction in scanning range due to lower thermal conductivity could possibly be compensated by the thermo-optic effect for group velocity. A matching scanning range between model and measurements would be a coincidence.

On the contrary, the non-linear model manages to compensate for the non-linearity reported in literature. With the thermal diffusivity scaled down by a factor 0.4, the non-linear model also compensates for the limited bandwidth. Although the ideal scanning range is 200 μm, Figure 5.8 has a flat region at a scanning range of 240 μm. The non-linear model can probably provide a flat frequency behaviour up to 5 kHz with a factor for thermal diffusivity slightly lower than 0.4. All in all, the corrected non-linear model has proved to increase the linearity and the bandwidth of the TODL dramatically. The line scanning rates achieved go up to 10 kHz, where literature reports values of $1 - 2$ kHz[6].

Chapter 6

Conclusions & outlook

The goal of this thesis project was to design the excitation and readout for a thermally driven Time-Domain Optical Coherence Tomography system. The excitation of the system comprises the characterisation of thermally driven ODL or Thermo-Optical Delay Line (TODL) in order to find the voltage excitation waveform that results in a linearly varying effective optical path length in the TODL.

The desired variation in effective optical path length has a triangular waveform, because a triangular waveform consists of two linear sections. However, this implies two points in the waveform where the waveform is not smooth. In other words, high frequencies dominate at the places where the waveform is not smooth and the TODL needs a high bandwidth to be able to follow the triangular waveform. Unfortunately, the bandwidth of the TODLs available is limited. The bandwidth of the TODLs can be extended by pre-emphasis of higher frequencies in the voltage excitation waveform. To apply this pre-emphasis, the power consumption and frequency behaviour have to be known. For this purpose, the required power and the frequency behaviour of the TODLs is modeled. Two other parameters are taken into account, being the membrane width and the ambient temperature.

Two models are presented that predict the optical behaviour of the TODL according to a certain voltage excitation waveform. One model is based on Fourier decomposition of the heat equation and is thus a linear model by definition. It uses constant values for the three most important properties of silicon, being the thermal conductivity, thermal diffusivity and the thermo-optic effect. The other model takes into account the non-linearities of the three properties mentioned. The heart of both models is the general heat conduction equation, which links the behaviour in the electrical domain to the optical behaviour are coupled through the thermal domain. To find the voltage excitation waveform corresponding to a desired optical behaviour, an iteration process is built around the models. The iteration process adjusts the input of the model until the desired optical behaviour is approximated within a certain accuracy. Given the ambient temperature and a membrane width, the iteration process generates a voltage excitation waveform that is pre-emphasised for higher frequencies.

The pre-emphasis only extends the bandwidth if the models are accurate. To verify the model and the pre-emphasis, a measurement setup has been designed. The measurement setup combines the excitation and readout of a TD-OCT imaging system based on the TODL. The core of the measurement setup is the readout of the optical signal coming from the TD-OCT system with the TODL in the sample arm and a scanning mirror in the reference arm. As a double-check of the model, the temperature of the membrane is measured via the platinum heater. By comparison of the temperature behaviour to the optical behaviour, deviations from the model can be assigned to specific model parameters.

The verification benefits from a multitude of measurements for a wide variety of input parameters. The flexibility of the measurement setup allows measurements to be taken for a wide range of input parameters by changing a few parameters in MATLAB$^{\circledR}$. The readout electronics are designed to change the TODL under test in a matter of minutes. To further ease the measurements, the whole measurement process is autonomous. Firstly, this can be exploited to reduce measurement errors. Multiple measurements with the same input parameters can be taken without any user intervention. Mean values and standard deviation

of the measurands are calculated automatically. Secondly, autonomous measurements are a first step to real-time OCT imaging.

Both models can be verified by comparing the measured scanning range and linearity to the desired triangular waveform. The linear model performs poorly for both. The scanning range shows an error of more than 50 %. Whereas the scanning range can be tuned by adjusting the power, the linearity cannot be compensated for. The conclusion to draw from the linear model is that thermal conductivity and diffusivity cannot be assumed to be constant.

This leaves us with the non-linear model. The measured scanning range is very close to the ideal case for low frequencies. At higher frequencies, the scanning range drops and also the linearity decreases rapidly. Inspection of the shape of the error between the ideal curve and the measured curve reveils that the membrane is behaving more slowly than predicted by the model. This implies that the values for thermal diffusivity, the rate of heat flow, in the model are too high. Lowering the thermal diffusivity in the model results in more pre-emphasis in the voltage excitation waveform.

The thermal diffusivity is scaled down by an empirical factor of 0.4x. Measurements taken at an excitation frequency of $5\,\text{kHz}$ now show a scanning range that corresponds to the predicted values. In terms of linearity, the non-linear model with corrected thermal diffusivity at $5\,\text{kHz}$ performs better than the uncorrected non-linear model at $1\,\text{kHz}$. This means that a TD-OCT imaging system based on a TODL can reach line scanning rates of $10\,\text{kHz}$. Line scanning rates reported in literature for the commonly used grating-based delay line go up to 1-$2\,\text{kHz}$.

Outlook

This thesis project was designed to be part of the Dental Drilling Sensory System, a prototype of a surgical drilling system enhanced with sensor feedback from the anatomical structures and tissue. The outlook is therefore split up into an outlook regarding the ODL and the outlook on the use of the device in the Dental Drilling Sensory System.

On modeling the TODL:

A lowered thermal diffusivity results in a more accurate model for higher frequencies. The question is how this lower thermal diffusivity can be explained. The answer could be in the layer of Silicon-Nitride that is on top of the membrane. The thermal diffusivity and conductivity of Silicon-nitride are lower than for silicon and the total diffusivity could be a weighted average of the properties of the two layers.

Further research of the interaction between the silicon membrane and the layer of Silicon-nitride may also give more insight in the thermal conductivity. Together with the thermo-optic effect for group velocity, this will clear up the discrepancy between the predicted thermal waveform and the measurements.

According to both models, there is a trade-off between power consumption and bandwidth. Furthermore, the power consumption in comparison with the membrane width indicates a constant power-width product. Unfortunately, a lack of measurements prevents a decent analysis of this relation. The exchange between power and bandwidth as a function of membrane width is interesting from a designer's point of view. With this relation at hand, the membrane width can be determined based on a requirement in either bandwidth or power.

Regarding the measurements that are already taken, there is more information to be extracted from the raw measurement data. The most interesting parameter to investigate is the FWHM bandwidth of the interference pattern, which is a measure for dispersion. As dispersion decreases the resolution of the system, further analysis gives insight in the dispersion as a function of e.g. temperature. Doing so, the resolution of the system can be determined. Using the insight gained, the resolution can be enhanced.

The iteration process starts to run into convergence problems for low values of the thermal diffusivity or for high frequencies. The reason for this is a startup effect that tries to create a temperature offset

instantaneously at $t = 0$. To improve the convergence, this startup effect has to be discarded before calculation of the error.

On the Dental Drilling Sensory System:

The measurement setup presented in chapter 4 is a first step to a real-time OCT imaging system that can be used in the Dental Drilling Sensory System without much physical adaptation. To some extent, the measurement setup already provides real-time imaging with a line rate of about 1 Hz. The limitations are mainly due to the fact that the DAC has no buffer, which results in a continuous stream of data on the USB bus. As mentioned, the excitation waveform does not change often. One excitation can easily be stored inside the FPGA. The FPGA can then drive a DAC. This saves a lot of traffic on the USB bus, which can be used for transmission of line scanning data. The FPGA can even take the ambient temperature out of the equations by measuring the ambient temperature and applying the corresponding excitation waveform from an array of excitation waveforms.

Also, MATLAB® does a lot of post-processing. In general, a lot of functionality can be shifted from MATLAB® into the FPGA. Once the excitation waveform is coming from the FPGA, triggering of all the data is fairly easy. Eventually, the FPGA should be capable of sending full frames to the computer.

For imaging purposes, a scanning range of 200 μm is small. The scanning range increases for higher power and longer devices, but this needs redesign of the TODL. An easier approach is the use of multiple passes. When the optical losses of mainly the chromatic dispersion compensation block are minimized, a fifth reflection might still give enough SNR. The scanning range increases to 1 mm, a reasonable range for imaging purposes.

References

[1] L. Ellies, "The incidence of altered sensation of the mental nerve after mandibular implant placement," *Journal of Oral Maxillofacial Surgery*, vol. 57, no. 12, pp. 1410–1412, 1999.

[2] C. Goodacre, G. Bernal, K. Rungcharassaeng, and J. Kan, "Clinical complications with implants and implant prostheses," *Journal of Prosthetic Dentistry*, vol. 90, no. 2, pp. 121–132, 2003.

[3] D. Huang, E. Swanson, C. Lin, and J. Schuman, "Optical coherence tomography," *Science*, vol. 254, pp. 1178–1181, 1991.

[4] M. E. Brezinski, G. J. Tearney, and B. E. Bouma, "Optical coherence tomography for optical biopsy," *Circulation*, vol. 93, pp. 1206–1213, 1996.

[5] A. Fercher, W. Drexler, C. Hitzenberger, and T. Lasser, "Optical coherence tomography - principles and applications," *Reports on Progress in Physics*, vol. 66, pp. 293–303, 2003.

[6] G. Tearney, B. Bouma, and J. Fujimoto, "High-speed phase- and group-delay scanning with a grating-based phase control delay line," *Optics Letters*, vol. 22, no. 23, 1997.

[7] E. M. Balbás, G. Pandraud, and P. French, "Rapid scanning delay line for optical coherence tomography based on the thermo-optic effect in silicon," *?*, 2008.

[8] G. Reed, *Silicon Photonics; an introduction*. John Wiley & Sons, 2004.

[9] D. Blackburn, "Temperature measurements of semiconductor devices - a review," *IEEE 20th SEMI-THERM Symposium*, 2004.

[10] R. Soref and B. Bennet, "Electrooptical effects in silicon," *IEEE Journal of Quantum Electronics*, vol. 23, no. 1, 1987.

[11] M. Ashegi, K. Kurabayashi, R. Kasnavi, and K. Goodson, "Thermal conduction in doped single-crystal silicon films," *Journal of Applied Physics*, vol. 91, no. 8, 2002.

[12] H. Shanks, P. Maycock, P. Sidles, and G. Danielson, "Thermal conductivity of silicon from 300 to 1400k," *Physical review*, vol. 130, no. 5, 1963.

[13] B. Bouma and G. Tearney, *Handbook of Optical Coherence Tomography*. Dekker, 2002.

[14] K. Kwong, D. Yankelevich, and K. Chu, "400-hz mechanical scanning optical delay line," *Optics Letters*, vol. 18, no. 7, 1993.

[15] R. Fork and F. A. Beisser, "Real-time intensity autocorrelation interferometer," *Applied Optics*, vol. 17, no. 22, 1978.

[16] Z. Yasa and N. Amer, "A rapid-scanning autocorrelation scheme for continuous monitoring of picosecond laser pulses," *Optics Communications*, vol. 36, no. 5, 1981.

[17] E. Choi, J. Na, and S. Ryu, "All-fiber variable optical delay line for applications in optical coherence tomography: feasibility study for a novel delay line," *Optics Express*, vol. 13, no. 4, 2005.

[18] R. Soref, J. Schmidtchen, and K. Petermann, "Large single-mode rib waveguides in gesi-si and si-on-sio$_2$," *IEEE Journal of Quantum Electronics*, vol. 27, no. 8, 1991.

[19] S. Pogossian, L. Vescan, and A. Vonsovici, "The single-mode condition for semiconductor rib waveguides with large cross section," *IEEE Journal of Lightwave Technology*, vol. 16, no. 10, 1998.

[20] A. Rickman, G. Reed, and F. Namavar, "Silicon-on-insulator optical rib waveguide loss and mode characteristics," *IEEE Journal of Lightwave Technology*, vol. 12, 1994.

[21] F. J. Morin and J. P. Maita, "Electrical properties of silicon containing arsenic and boron," *Phys. Rev.*, vol. 96, pp. 28–35, Oct 1954.

[22] M. A. Green, "Intrinsic concentration, effective densities of states, and effective mass in silicon," *Journal of Applied Physics*, vol. 67, no. 6, pp. 2944–2954, 1990.

[23] G. Ghosh, "Temperature dispersion of refractive indices in crystalline and amorphous silicon," *Applied Physics Letters*, vol. 66, no. 26, 1995.

[24] G. Cocorullo, F. G. D. Corte, and I. Rendina, "Temperature dependence of the thermo-optic coefficient in crystalline silicon between room temperature and 550 k at the wavelength of 1523 nm," *Applied Physics Letters*, vol. 74, no. 22, 1999.

[25] E. M. Balbás, G. Pandraud, and P. French, "Miniature optical coherence tomography system based on silicon photonics," *Coherence Domain Optical Methods and Optical Coherence Tomography in Biomedicine XII*, vol. 6847, p. 68470S, 2008.

[26] J. Hartman, *PDB100 Series Operation Manual*, 2007.

Acknowledgement

In February 2009 I started my thesis project on the 13th floor of the Faculty of EEMCS, at the Electronic Instrumentation Laboratory. A little more than a year I spent on the design of a system that should get the best out of the TODL. And with great pleasure, thanks to a lot of people.

First of all, I'd like to thank Eduardo Margallo, my daily supervisor and mentor. We have been working closely together for the whole year. We had a lot of discussions on the progression and the optimalisation of the device and the measurement system. In my opinion, the synergy worked out nicely.

Furthermore, I thank Paddy French for supervising the project and Dedy Wicaksono for his support in the beginning phase. His way of keeping a log of a project has proven to be extremely helpfull. A great help in the mechanical design was my father, René Geljon. Together we fabricated the brackets for the TODLs and we made modifications to the heatsink. Another form of mechanical design has been done in the form of the chromatic dispersion blocks. I thank Henk van Zeijl and Timon Grob for their contributions to that part.

In terms of advice, I'd like to thank the technical staff of the Electronics Instrumentation Laboratory. Not only were they good company for a chat and coffee, they also helped out with instrumentation equipment from time to time.

I would like to thank 'EI people' for offering me a great time while working on my thesis project. In particular, my roommates Agung Purniawan and Gayathri Nampoothiri, and CK Yang for dropping by regularly. The many chats and discussions I had with people from EI Lab, on a wide variety of topics, while walking from the 13th to the 14th, while getting coffee, during lunch, et cetera, made my thesis project a pleasent experience.

A special thanks is awarded to 'de Oude Dame', the personification of the study association ETV, representing all the people who have ever contributed to her legacy. Over one hundred years old, the experience and traditions she gathered has added to my personal skills on both a scientific and a social level.

Last but most important, my parents. Their unlimited trust and support gave me the ability and the freedom to finish my studies in seven and a half years. A great deal of that time I spent on characterising myself and improvement on the models of life. A invaluable experience.

Gain-phase characterisation of readout-board

To verify the proper functioning of the readout-board, a gain-phase analysis has been performed with the help of the HP 4194A Impedance/Gain-Phase Analyzer. The analyzer is compatible with GPIB, which allows Labview to take automated measurements. The block diagram from Labview is shown in Figure 1. The block diagram produces all the measurement settings that are necessary to perform the gain-phase analysis. The results are shown on-screen and saved in a file. The files are later imported in MATLAB®to create Figures 2 to 4.
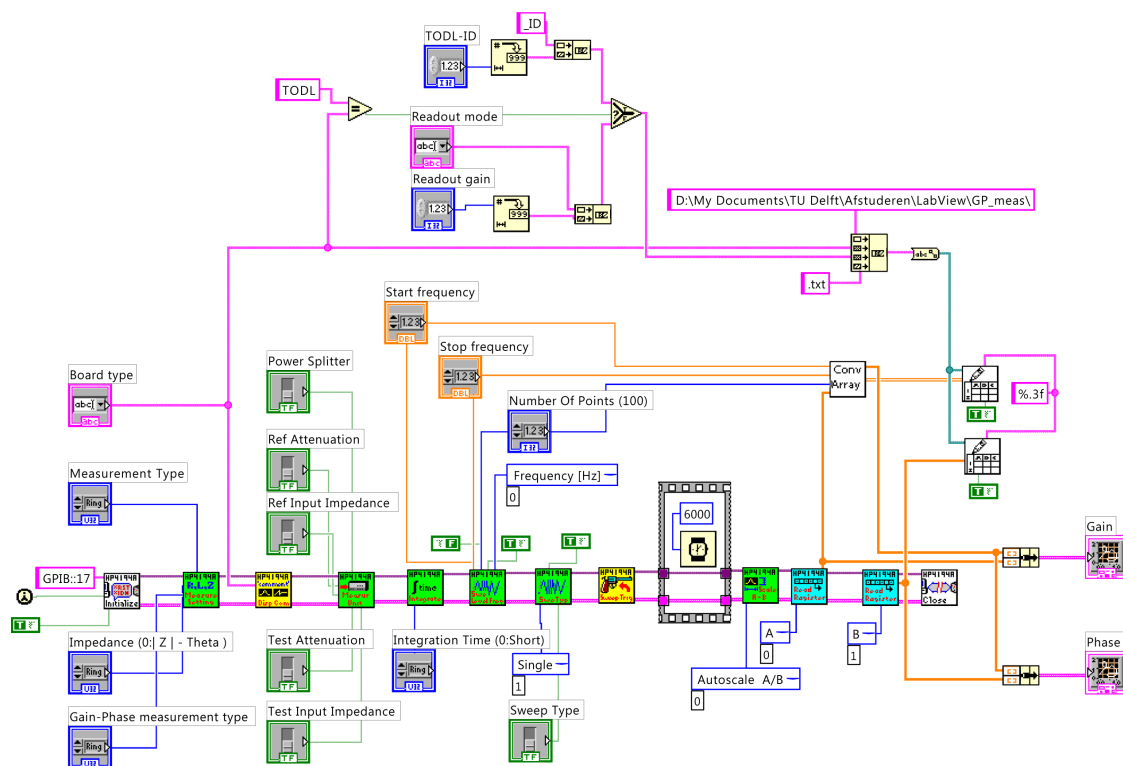

Figure 1. Labview schematic for control of the HP4194A Gain-phase analyzer

Figure 2 shows the gain-phase characteristics for the voltage channel with the gain settings that are used most frequently. The gain mentioned in the legend is the value taken from the board design. The measured gain is shown in the graph. Figure 3 shows the gain-phase characteristics for the current channel. Besides the gain and the phase, the phase difference between the voltage channel and the current channel is of special interest. The phase difference for the three gain settings are shown in Figure 4. The phase difference is less than $0.1\,^\circ$ for the whole frequency range.
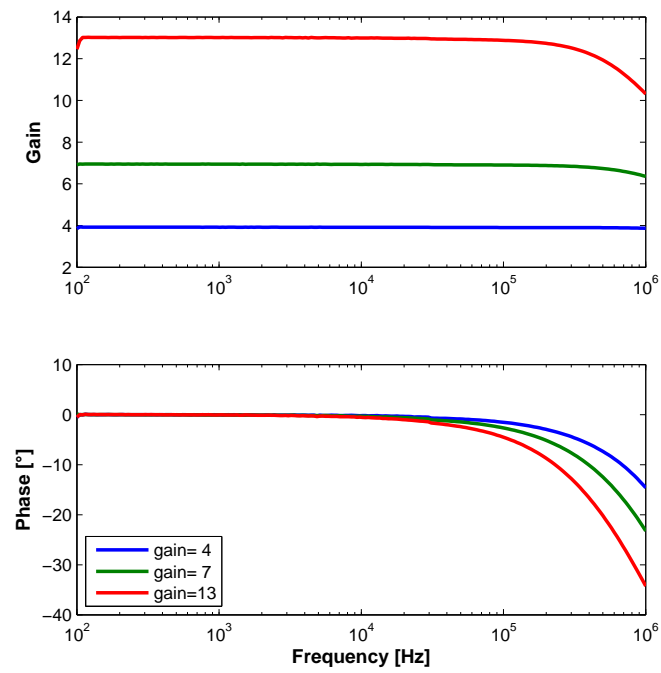
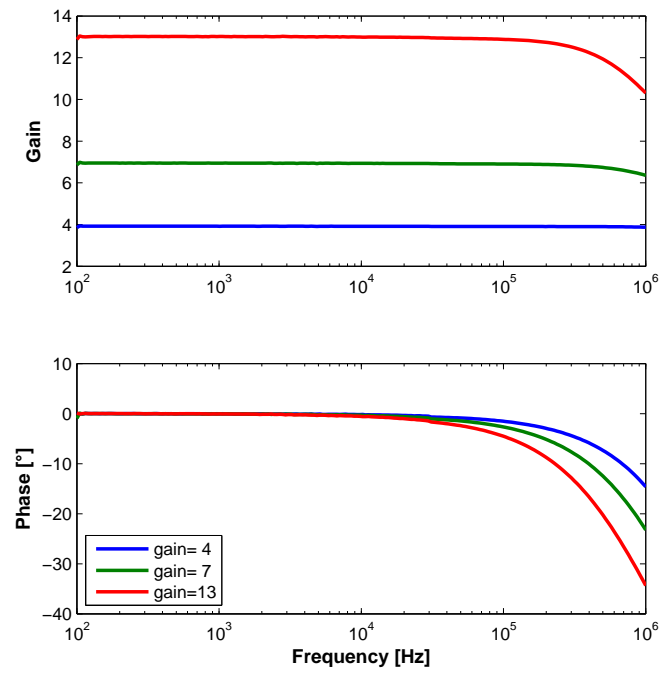**Figure 2.** Gain-phase analysis for the voltage channel on the readout-board

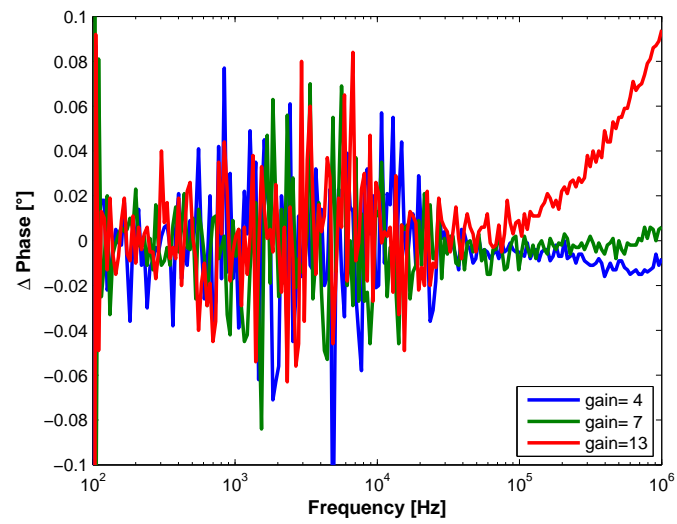**Figure 3.** Gain-phase analysis for the current channel on the readout-board

Figure 4. Phase difference between the voltage channel and the current channel